Green Chemistry

ROYAL SOCIETY OF CHEMISTRY

PAPER

View Article Online
View Journal

Cite this: DOI: 10.1039/d6gc02407f

Dual hydrogen-buffer and interfacial spillover effects boosting bimetallic catalysts for mild-condition guaiacol hydrodeoxygenation

Reem Shomal and Ying Zheng *

Received 23rd April 2026,
Accepted 22nd June 2026

DOI: 10.1039/d6gc02407f

rsc.li/greenchem

Regulating hydrogen activation and transport is an effective strategy for improving bimetallic catalyst performance in the hydrodeoxygenation (HDO) of lignin-derived phenolics under mild conditions. Herein, we report a dual hydrogen-regulation strategy that integrates silicotungstic acid (SiW_{12}) with a sequentially Ni–Ru bimetallic catalyst to control hydrogen availability and reaction selectivity in aqueous-phase HDO. Mechanistic investigations combining electrochemical measurements, UV–Vis spectroscopy, *in situ* DRIFTS, and hydrogen adsorption analysis demonstrate that SiW_{12} performs a dual function. In solution, it acts as a molecular hydrogen buffer that facilitates hydrogen transfer from the gas–liquid interface into the bulk liquid while mitigating mass-transfer limitations. During reaction, *in situ* modification of the Ni–Ru/TiO_2 interface by SiW_{12} generates interfacial sites that promote hydrogen spillover and proton-assisted C–O bond polarization. This cooperative interaction between homogeneous redox buffering and heterogeneous interfacial catalysis establishes a dynamic catalytic environment integrating H_2 activation, hydrogen transport, acid-assisted bond cleavage, and suppression of carbonaceous deposition during aqueous-phase HDO. Noble-metal on Ni/TiO_2 studies (Pt, Ru, Pd) further reveal that hydrogen chemisorption strength and metal–support interactions govern hydrogen mobility and buffering efficiency, resulting in the activity trend Ni–Pt > Ni–Ru > Ni–Pd, while the Ni–Ru configuration provides the optimal balance between hydrogen activation and selective hydrogenation to cyclohexanol. Collectively, under mild conditions (0.5 MPa H_2, 125 °C), the catalyst delivered 59.8% guaiacol conversion and 69.3% cyclohexanol selectivity within 1 h. This work introduces a dynamic hydrogen-management paradigm for one-pot HDO to enable energy-efficient biomass upgrading under mild multiphase reaction conditions.

Green foundation

1. This study introduces a hydrogen-transfer-regulated catalytic strategy for biomass upgrading, where hydrogen buffering, interfacial hydrogen spillover, and bimetallic catalyst modulation cooperatively regulate hydrogen delivery across gas–liquid–solid interfaces, enabling selective one-pot hydrodeoxygenation under mild conditions.
2. The catalytic system enables selective hydrodeoxygenation of lignin-derived phenolics under significantly milder conditions (95 °C and 0.5 MPa H_2) compared with conventional HDO processes that typically require 200–350 °C and multi-MPa hydrogen pressures, improving hydrogen utilization efficiency while reducing energy demand.
3. Future research could focus on improving catalyst recyclability, integrating alternative hydrogen sources, and scaling the hydrogen-buffer strategy for direct upgrading of real bio-oil mixtures and other triphasic hydrogenation systems.

1. Introduction

The development of catalytic technologies capable of converting renewable biomass into value-added fuels and chemicals has become increasingly important in the transition toward sustainable energy systems.[1,2] Catalytic hydrodeoxygenation (HDO) of lignin-derived phenolics plays a central role, as it removes oxygen functionalities and improves the stability, energy density, and fuel compatibility of bio-derived streams.[3–5] Noble-metal catalysts such as Pt, Ru, Rh and Pd are traditionally considered highly effective for HDO due to their excellent hydrogen-activation capability and balanced hydrogenation–deoxygenation activity.[6,7] However, their practical application is constrained by high cost, limited availability, and the requirement for elevated hydrogen pressures, which restricts large-scale and energy-efficient implementation.[8,9]

Department of Chemical and Biochemical Engineering, Western University of Ontario, 1150 Richmond Street, London, Ontario N6A 3K7, Canada.
E-mail: ying.zheng@uwo.ca

To address these limitations, bimetallic Ni–M (M = Ru, Pd, Pt) catalysts have been widely explored as a strategy to enhance catalytic performance while reducing noble-metal usage.[6,7,9,10] In these systems, nickel functions as the primary hydrogenation center while electronically modulating the secondary metal.[11] Charge transfer at the Ni–M interface alters the d-band structure, regulating hydrogen adsorption strength and reactivity. Moreover, at low noble-metal loading, heteroatomic Ni–M interfacial sites dominate, while the surrounding Ni matrix stabilizes the secondary metal and suppresses segregation.[10–12] Furthermore, the sequence of metal deposition strongly influences interfacial bonding and catalytic behaviour by governing the architecture of active sites and the extent of metal–metal interaction.[12] This cooperative interaction between two metals enables more controlled hydrogen activation and utilization, promoting selective C–O bond activation over non-selective hydrogenation.[9] Despite these advances, achieving selective HDO of lignin-derived phenolics under mild thermal conditions remains highly challenging.[13–17] In conventional bimetallic catalyst-assisted HDO systems, reactive hydrogen species are generated primarily through dissociative adsorption of hydrogen gas (H_2) on metal surfaces under elevated temperatures (200–350 °C) and H_2 pressure (2–10 MPa), forming surface-bound hydrogen species (M–H*) that participate in both hydrogenation and hydrogenolysis reactions depending on catalyst properties and adsorption configurations, although hydrogenation pathways are often kinetically favoured under these conditions.[18] The harsh conditions required for HDO arise from the thermodynamically demanding cleavage of aromatic C–O bonds, which possess high bond dissociation energies (~468 kJ mol^{-1}).[19] These severe conditions often accelerate condensation reactions and catalyst deactivation.[1,20,21] The challenge is further magnified in multiphase HDO systems due to the inherently low solubility and slow diffusion of hydrogen gas in water, which constrain the continuous supply of reactive hydrogen species to the catalytic interface under mild conditions.[6,19,22] Because hydrogen plays a central role in aromatic ring hydrogenation, oxygen removal, and maintaining metal sites in their reduced state, enhancing hydrogen availability and transport under mild conditions is a key requirement for practical multiphase HDO processes.[13,23] These limitations indicate that improving hydrogen activation in bimetallic catalysts alone is insufficient; instead, the key lies in controlling how hydrogen is transferred, distributed, and utilized at the catalytic interface. Studies inspired by electrochemical systems show that reaction selectivity depends strongly on the hydrogen-transfer mode. When hydrogen is delivered through proton-coupled electron transfer (PCET), C–O bond cleavage is favoured because proton and electron transfer occur cooperatively, lowering the barrier for bond polarization.[18,24,25] Translating this concept to bi-metallic catalysis suggests that regulating hydrogen delivery *via* adsorbed hydrogen, spillover hydrogen, or proton-assisted pathways, can provide a powerful strategy to control HDO selectivity at mild reaction conditions.[25]

Heteropoly acids (HPAs), particularly Keggin-type structures such as phosphotungstic acid (PWA) and silicotungstic acid (SiW_{12}), have attracted significant attention due to their strong Brønsted acidity, reversible redox behavior, and high thermal stability.[26,27] Among them, SiW_{12} can function as a reversible hydrogen buffer by cycling between the $[SiW_{12}]^{4-}/[SiW_{12}]^{5-}$ redox pair to mediate proton–electron transfer (H^+/e^-) at the catalytic interface.[21,28,29] Owing to its redox potential being close to that of the H^+/H_2 couple ($E°$ = −0.05 V *vs.* NHE), SiW_{12} can reversibly store and transport reactive hydrogen equivalents from the gas–liquid interface into the bulk liquid phase and subsequently to the catalyst surface.[30] This behavior mitigates hydrogen mass-transfer limitations that typically constrain multiphase HDO systems, enabling more efficient hydrogen utilization under mild conditions.[21,28,30] Wei Liu *et al.* reported that combining SiW_{12} with Pt/C enabled lignin bio-oil upgrading below 100 °C under near-ambient hydrogen pressure, achieving high hydrocarbon yields through efficient hydrogen transfer and proton coupling.[21] Gao *et al.* showed that Pt–HPA catalysts exhibit high HDO efficiency due to strong metal–HPA electronic synergy.[26] Similarly, Kozhevnikov and co-workers demonstrated that Cs-HPA-supported Pt catalysts effectively catalyze deoxygenation of ethers, esters, and ketones under mild conditions,[31–34] while Mizuno *et al.* further confirmed the bifunctional advantages of combined metal–acid catalysis.[35] Despite these advances, the interaction between SiW_{12} and bimetallic Ni catalysts remains insufficiently understood. In particular, how different bimetallic systems (Ni–Pt, Ni–Pd, Ni–Ru) influence the formation and transfer of reactive hydrogen species, hydrogen mobility, and acid–metal cooperation in the presence of SiW_{12} remains unclear. Elucidating these interactions is essential for designing efficient catalytic systems capable of achieving selective multiphase HDO of lignin-derived phenolics under mild conditions.

Motivated by the need to regulate hydrogen transfer rather than merely hydrogen activation in multiphase HDO systems. Herein, we developed a dual hydrogen-buffer and interfacial spillover catalytic system for the selective upgrading of lignin-derived phenolics under mild multiphase reaction conditions. The system couples Ni–M (M = Ru, Pt, Pd) bimetallic catalysts, which serve as hydrogen activation sites, with soluble SiW_{12} acting as a reversible hydrogen-transfer mediator. Comparative studies reveal that bimetallic cooperation facilitates efficient H_2 activation and accelerates SiW_{12} reduction, thereby improving guaiacol conversion and promoting deep deoxygenation. Post-reaction analyses indicate *in situ* modification of the catalyst surface by SiW_{12}, forming an interfacial metal–acid structure that regulates hydrogen adsorption and spillover. Among the catalysts investigated, Ni–Ru provides the most effective balance between hydrogen activation and controlled hydrogen delivery, resulting in superior cyclohexanol selectivity. Structure–function relationships are elucidated using H_2-TPR/TPD, TEM-EDS, XPS, and *in situ* DRIFTS, supported by electrochemical measurements and UV–Vis spectroscopy evidence of SiW_{12} redox cycling. Overall, this work demonstrates a hydrogen-transfer-regulated HDO mechanism enabled by the synergistic interaction between bimetallic catalysts and a reversible hydrogen buffer, providing a new framework for designing catalytic systems for sustainable bio-oil upgrading.

2. Methodology and catalyst preparation

2.1 Preparation of the catalyst

To prepare the catalysts with varying Ni loadings, an incipient wetness impregnation method was employed, following procedures reported in the literature with certain modifications.[36] First, a precursor solution of nickel nitrate hexahydrate (Ni $(NO_3)_2 \cdot 6H_2O$, 25 mL) was prepared and slowly added dropwise onto a commercially purchased TiO_2 support (Aeroxide P25). The mixture was continuously stirred for 4 hours to promote even dispersion, followed by drying at 100 °C for 12 hours. The dried samples were then calcined at 450 °C under a nitrogen atmosphere for 4 hours (ramping rate of 5 °C min^{-1}) under the flowrate of (40 mL min^{-1}), and subsequently reduced in a hydrogen flow (40 mL min^{-1}) at 500 °C for 4 hours to activate the catalysts before being used. After calcination, the 3wt% nickel-loaded TiO_2 was subjected to a second impregnation step to introduce ruthenium (Ru), platinum (Pt), or palladium (Pd) using their respective precursors, ruthenium chloride hydrate ($RuCl_3 \cdot xH_2O$) solution for Ni–Ru/TiO_2 (0, 0.3, 0.5, 0.7, and 1 wt%), tetraamine platinum(II) nitrate $[Pt(NH_3)_4(NO_3)_2]$ for Ni–Pt/TiO_2 (1 wt%), and palladium(II) chloride ($PdCl_2$) for Ni–Pd/TiO_2 (1 wt%). The impregnated samples were stirred for 4 hours, dried at 100 °C for 12 h, and calcined at 400 °C for 4 h under a nitrogen atmosphere, and reduced at 450 °C under hydrogen flow (40 mL min^{-1}) for 2 hours. The final catalysts were stored in a desiccator before being used in catalytic HDO reactions. The details of the chemicals used are provided in the SI section.

2.2 Catalytic test

The HDO activity of the synthesized catalysts was evaluated in a miniature, magnetically stirred, high-temperature and high-pressure batch reactor (JGF-50 mL, Shanghai Jie Ang Instrument Co., Ltd). The experimental procedure was adapted from Wei Liu *et al.*[21] and our previous work.[30] Initially, SiW_{12} was dissolved in 9 mL of ultrapure water (18 MΩ cm) to obtain final concentrations of 0.008–0.05 mol L^{-1}. The catalyst 0.04–0.12 g was then dispersed in the solution and introduced into the reactor. To eliminate residual air, the reaction system was purged with H_2 gas three times. The SiW_{12}-containing solution was then pre-reduced to equilibrium for 15 min under a continuous H_2 flow (100 mL min^{-1}). Subsequently, 0.25–2 mL of pure guaiacol was added to the reactor. The reaction parameters were set to H_2 pressures of 0.25–2 MPa, temperatures of 35–125 °C, and stirring rates of 550–1000 rpm. The reaction proceeded for 0.5–8 h before being rapidly quenched to 30 °C using an ice bath. The reaction mixture, containing both products and catalyst, was collected in a 50 mL conical tube. The organic phase was extracted twice using 5 mL of pure DCM, centrifuged at 12 000 rpm for 5 min, and the resulting organic layer was transferred to a 15 mL conical flask. Subsequently, 20 μL of pure *n*-octane was added as an internal standard. A 1 mL aliquot of the product was filtered through a 0.22 μm PTFE syringe filter prior to analysis. Quantitative composition was determined using flame ionization detection gas chromatography (FID-GC, Shimadzu GC-2014), while qualitative characterization was performed using gas chromatography–mass spectrometry (GC-MS) (Clarus 680 GC-MS). Gaseous products were characterized using a TCD-FID-equipped GC system (Shimadzu GC-2014). The catalyst performance was quantified based on conversion (%) and product selectivity (%) using eqn (1) and (2), respectively.

$$\text{Guaiacol conversion}\,(\%) = \frac{\text{feed moles}_{\text{in}} - \text{feed moles}_{\text{out}}}{\text{feed moles}_{\text{in}}} \times 100 \tag{1}$$

$$\text{Product selectivity}\,(\%) = \frac{\text{mole of product}\,(n_i)}{\sum \text{total moles of products}\,(n_{\text{total}})} \times 100. \tag{2}$$

2.3 Characterization

The structural properties of the catalysts were characterized using several complementary analytical techniques. X-ray Diffraction (XRD) patterns were obtained with a Rigaku SmartLab, HyPix-3000 diffractometer to identify the crystalline phases. The morphology and dispersion of nanoparticles were examined by Transmission Electron Microscopy (TEM) using a JEOL-JEM-2100F instrument. The textural properties, including surface area, pore volume, and pore size distribution, were analyzed through Brunauer–Emmett–Teller (BET) and Barrett–Joyner–Halenda (BJH) methods on a Quantachrome NovaWin™ (version 11.03) system. X-ray Photoelectron Spectroscopy (XPS) was performed on an ESCALAB 250Xi spectrometer to evaluate surface composition, elemental interactions, and the oxidation states of active species. Temperature-Programmed Reduction (H_2-TPR) measurements were carried out using a Micromeritics Chemisorb 2750 equipped with a Thermal Conductivity Detector (TCD). For this analysis, (50 mg) of catalyst was pretreated under an argon flow (20 mL min^{-1}) at 250 °C for 1 h, cooled to 50 °C, and subsequently reduced in 5 vol% H_2/Ar (20 mL min^{-1}) while heating to 800 °C at 10 °C min^{-1}. Hydrogen adsorption–desorption behavior was examined by (H_2-TPD) using the same instrument. A (100 mg) portion of the catalyst was first activated *in situ* under a H_2 gas (20 mL min^{-1}) at 450 °C for 2 h. The sample was then cooled to 50 °C in an argon atmosphere and exposed to H_2 gas for 45 min to ensure complete surface saturation. To eliminate weakly adsorbed hydrogen, the system was subsequently purged with argon for 15 min. Finally, H_2-TPD was carried out by heating the sample from 50 °C to 800 °C at a rate of 10 °C min^{-1} under a continuous argon flow

(20 mL min^{-1}), while the evolved hydrogen was quantitatively measured using a TCD. Acidic properties were determined through NH_3-TPD. The catalyst (100 mg) was first reduced under H_2 (50 mL min^{-1}) at 450 °C for 2 h, cooled to 50 °C, and exposed to NH_3/He (30 mL min^{-1}) for 1 h to achieve adsorption saturation. Physically adsorbed ammonia was then purged with N_2 for 30 min. Desorption was carried out between 50 °C and 700 °C at 10 °C min^{-1} under N_2 flow, and the effluent gases were analyzed with a TCD. O_2-TPO analysis was performed to evaluate the nature and oxidation behavior of carbonaceous species deposited on the spent catalysts. The catalyst sample (50 mg) was first pretreated under an argon flow (40 mL min^{-1}) at 250 °C for 2 h, followed by cooling to 50 °C. Subsequently, the sample was exposed to a 10 vol% O_2/Ar gas mixture generated by external gas mixing (31.5 mL min^{-1} Ar and 3.5 mL min^{-1} O_2; total flow rate = 35 mL min^{-1}) prior to entering the instrument, while the flow rate inside the instrument was maintained at 20 mL min^{-1}. The temperature was then increased from 50 °C to 800 °C at a heating rate of 10 °C min^{-1}, and the effluent gases were monitored using a TCD. *In situ* Diffuse Reflectance Infrared Fourier Transform Spectroscopy (DRIFTS) measurements were performed on a Thermo Scientific Nicolet iS50 FT-IR spectrometer equipped with an MCT detector and a high-temperature reaction cell fitted with a ZnSe window. Prior to spectral acquisition, 50 mg of catalyst was pretreated under H_2 (30 mL min^{-1}) at 450 °C for 2 h. Subsequently, 20 μL of guaiacol was introduced at room temperature and equilibrated for 10 min. DRIFTS spectra were collected every 5 min at a resolution of 4 cm^{-1} with 32 scans under a continuous H_2 flow (30 mL min^{-1}) while the temperature increased from 100 °C to 150 °C at 10 °C min^{-1}. Spectral data were processed using OPUS software.

2.4 Electrochemical tests

For the electrochemical experiments, the solution consisted of SiW_{12} with a concentration (0.012 mol L^{-1}), and 0.08 g of catalyst was introduced in 20 ml of water. A platinum wire functioned as the working electrode, paired with an Ag/AgCl reference electrode connected through a salt bridge. This configuration was used to monitor the potential behavior during the interaction of SiW_{12}, hydrogen gas and Ni–Ru/TiO_2, Ni–Pt/TiO_2 and Ni–Pd/TiO_2 catalysts having different metal ratios. Measurements of the potential difference between the working and reference electrodes were carried out using a GAMRY Interface 1010 E electrochemical workstation (Model 40005) at room temperature and room pressure in a 25 mL electrochemical cell. Throughout the test, hydrogen gas was supplied continuously to the cell at (50 mL min^{-1}), while the mixture was stirred at 800 rpm. The measured potentials were converted to the normal hydrogen electrode (NHE) scale using: $E_{NHE} = E_{Ag/AgCl} + 0.22$ V where E_{NHE} denotes the potential relative to the NHE reference. Cyclic voltammetry (CV) was also carried out on the same instrument using an Ag/AgCl reference electrode, an 8 mm glassy carbon working electrode, and a 15 mm × 15 mm platinum plate as the counter electrode. The experiments were conducted in (0.025 mol L^{-1}) SiW_{12} solution at ambient temperature with a scan rate of 100 mV s^{-1}. All potentials were referenced to the NHE scale as previously described.

3. Results and discussion

3.1 Characterizations and catalyst structure

The impact of noble metal (Pt, Ru, and Pd) incorporation into 3Ni/TiO_2 on the reduction behavior of the catalysts was investigated using H_2-TPR. For the 3Ni/TiO_2 catalyst (Fig. 1a), a significant reduction peak at 440 °C was observed, attributed to the interaction between NiO and the TiO_2 surface, with a shoulder peak at 340 °C corresponding to amorphous NiO without support interaction.[37] When Ru was added to the 3Ni/TiO_2 catalyst, as in the 3Ni1Ru/TiO_2 sample (Fig. 1a), the reduction profile shifted significantly. A sharp peak centered at 250 °C was observed, corresponding to the reduction of RuO_2 to Ru^0, while the region between 250 °C and 380 °C suggested the reduction of bimetallic species. Notably, the addition of Ru promoted the reduction of Ni to lower temperatures, from 440 °C (for 3Ni/TiO_2) to 380 °C, demonstrating a synergistic effect of Ru in enhancing Ni reduction.[38] This promotion of Ni reduction by Ru^0 has been previously reported, and is likely due to hydrogen spillover and enhanced hydrogen adsorption–desorption processes between the noble metal and metal oxide support.[39,40] In this mechanism, dissociated hydrogen species migrate from the noble metal to the surface of NiO, thereby facilitating the reduction at lower temperatures.[41] In addition, the narrower distribution of peaks associated with RuO_2 species in 3Ni1Ru/TiO_2 indicates better dispersion of Ru, likely resulting in a more efficient catalytic system. Pd incorporation presents a distinctly different reduction behavior. In 3Ni1Pd/TiO_2, the H_2-TPR profile shown in (Fig. 1a), begins with a reverse peak at around 100 °C, characteristic of hydrogen uptake on reduced Pd at room temperature, which is consistent with the formation of PdHx species.[42] This initial hydrogen absorption is followed by broad reduction events between 260 and 380 °C, attributed to the stepwise reduction of PdO and the formation of Ni–Pd interaction phases. Beyond 500 °C, an additional broad feature emerges, indicative of TiO_2 reduction facilitated by the presence of Ni–Pd, suggesting strong metal–support interactions.[43,44] The complexity of this reduction pattern reflects the multifaceted chemistry of Pd and underscores its intimate interplay with both Ni and the TiO_2 support. In contrast, Pt incorporation adds another dimension to the reducibility of 3Ni/TiO_2, shown in (Fig. 1a). The 3Ni1Pt/TiO_2 catalyst exhibits reduction peak around 240 °C, corresponding to oxidized Pt species and Pt–support boundary sites. A subtle shoulder at 350 °C indicates direct Ni–Pt interactions, while a pronounced peak at 430 °C is assigned to the reduction of NiO.[45] Compared with the base catalyst 3Ni/TiO_2, all noble metals improved reducibility, but Ru provided the most pronounced promotion, Pd induced complex metal–support effects, and Pt offered intermediate behavior. In addition, it

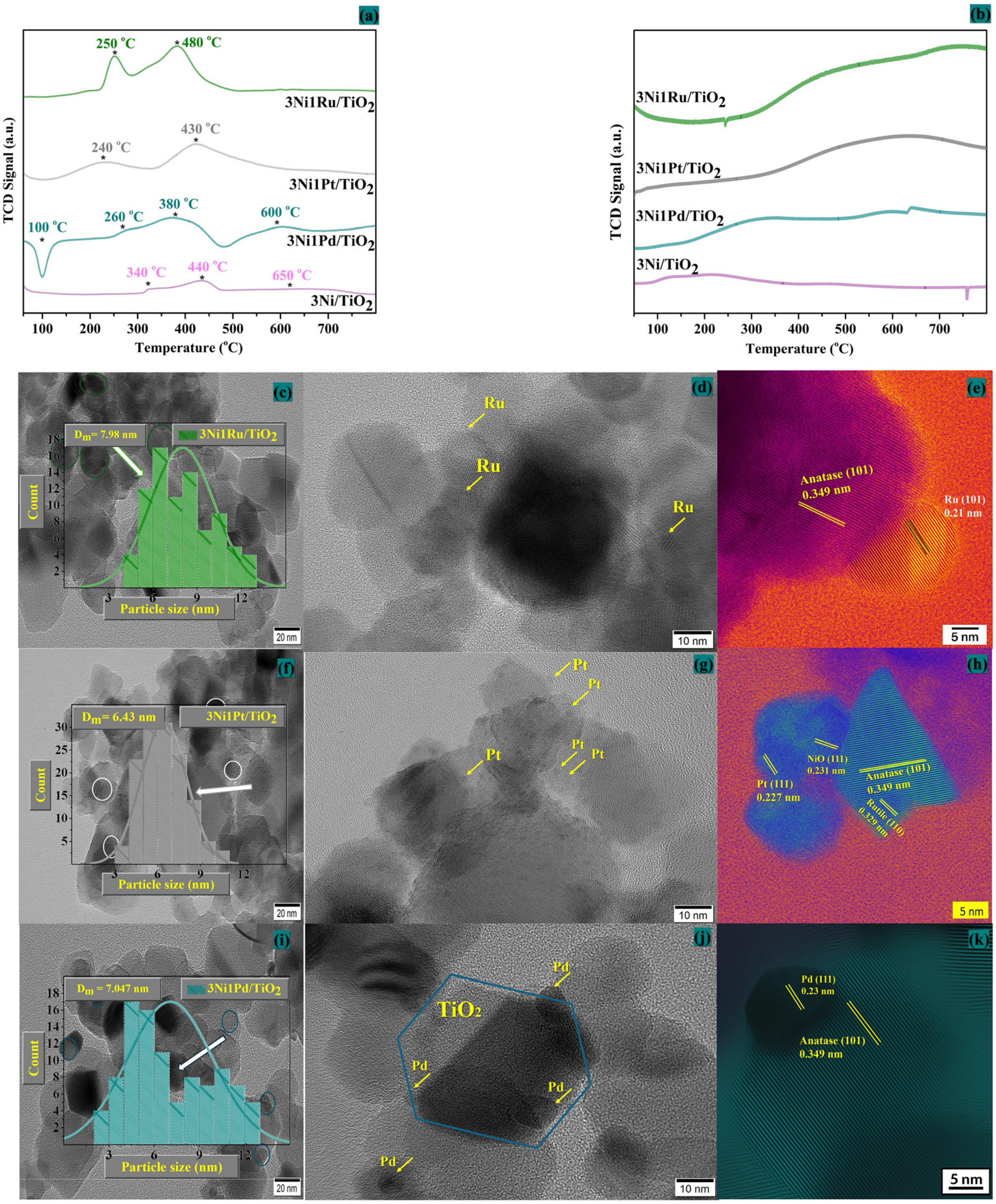

Fig. 1 (a) H_2-TPR analysis of bimetallic catalysts. (b) H_2-TPD analysis of bimetallic catalysts. (c–e) HTREM images of fresh 3Ni1Ru/TiO_2 with 20 nm, 10 nm, and 5 nm scale bars, and showing the mean particle size. (f–h) Display 3Ni1Pt/TiO_2 with 20 nm, 10 nm, and 5 nm scale bars, with showing the average particle size. (i–k) Show 3Ni1Pd/TiO_2 with 20 nm, 10 nm, and 5 nm scale bars with the mean particle size.

indicates that the metal–support interaction strength follows the order 3Ni/TiO_2 > 3Ni1Pd/TiO_2 > 3Ni1Ru/TiO_2 > 3Ni1Pt/TiO_2, with Pd and Ru promoting stronger Ni–TiO_2 interactions compared to Pt.

H_2-TPD profiles of the bimetallic 3Ni/TiO_2 catalysts (Fig. 1b) reveal that noble-metal incorporation markedly alters hydrogen adsorption–desorption behavior. The monometallic 3Ni/TiO_2 catalyst exhibits multiple hydrogen adsorption sites ranging from weak to strong adsorption, with a total hydrogen uptake of 3.92×10^{-3} mmol (Fig. S1 and Table S1). In contrast, 3Ni1Ru/TiO_2 displays a pronounced and broad high-temperature desorption region extending above 400 °C, indicative of strongly bound hydrogen species, with a total hydrogen uptake of 4.56×10^{-2} mmol, as shown in (Fig. S2 and Table S1). The 3Ni1Pd/TiO_2 catalyst exhibits predominantly low- to mid-temperature hydrogen desorption, indicating the presence of weakly bound and highly mobile surface hydrogen species that are readily available for hydrogenation reactions, with a total hydrogen uptake of 2.55×10^{-2} mmol (Fig. S3 and Table S1). Meanwhile, 3Ni1Pt/TiO_2 shows a broader desorption profile with enhanced mid-temperature features, suggesting the presence of weak to strong chemisorbed hydrogen associated with modified Ni electronic properties, with a reported total hydrogen uptake of 5.83×10^{-2} mmol (Fig. S4 and Table S1). Overall, the increase in hydrogen binding strength and stability follows the order Ni–Pd < Ni–Pt < Ni–Ru, while the total hydrogen adsorption follows the order Ni–Pd < Ni–Ru < Ni–Pt.

HRTEM-HAADF and EDS analyses were employed to elucidate how Pt, Ru, and Pd incorporation modulates particle size, dispersion, and elemental distribution in $3Ni/TiO_2$ catalysts (Fig. 1). For the $3Ni1Ru/TiO_2$ catalyst (Fig. 1c–e), HRTEM images reveal a relatively broad nanoparticle size distribution ranging from 5.5 to 13 nm, with an average diameter of approximately 7.98 nm (Fig. 1c). EDS elemental mapping (Fig. S5) confirms the homogeneous distribution of Ni and Ru within the nanoparticles, indicating effective co-deposition and uniform composition throughout the catalyst matrix, with no evidence of large-scale aggregation or phase separation.[46] In comparison, the $3Ni1Pt/TiO_2$ (Fig. 1f–h) and $3Ni1Pd/TiO_2$ (Fig. 1i–k) catalysts exhibited relatively lower metal dispersion, accompanied by slight nanoparticle agglomeration. EDS elemental mapping further confirmed the homogeneous distribution of Ni and Pt or Pd within the nanoparticles, as shown in (Fig. S6 and Fig. S7), respectively. and average particle sizes of 6.43 nm and 7.05 nm, respectively. All bimetallic catalysts exhibit smaller particle sizes than the monometallic Ni catalyst of particle size of 14.58 nm (Fig. 2d). It reported that noble-metal incorporation promotes a reduction-assisted effect that facilitates the formation of Ni–M bimetallic nanoparticles.[47] Accordingly, the average particle size follows the order $3Ni1Pt/TiO_2 < 3Ni1Pd/TiO_2 < 3Ni1Ru/TiO_2 < 3Ni/TiO_2$, while metal dispersion decreases in the order $3Ni1Ru/TiO_2 > 3Ni1Pt/TiO_2 > 3Ni1Pd/TiO_2$ with $3Ni1Ru/TiO_2$ exhibiting the highest dispersion. This trend is consistent with the H_2-TPR results in (Fig. 1a). FFT analysis identifies lattice fringes with spacings as shown in (Fig. 1e) of 2.31 Å and 2.10 Å, corresponding to the (111) plane of face-centered cubic Ni (JCPDS 004-0850) and the (101) plane of hexagonal close-packed Ru (JCPDS 006-0663), respectively.[36] In addition, the measured interplanar spacings are consistent with reported values for Ni (0.204 nm), Pt (0.227 nm), Pd (0.230 nm), and NiO (0.231 nm), confirming the formation of crystalline metallic and oxide nanoparticles within the catalyst system (Fig. 1h and k).

As our results suggest, $3Ni1Ru/TiO_2$ exhibits hydrogen-buffer-assisted HDO performance comparable to that of $3Ni1Pt/TiO_2$. Given that chemisorption characteristics and metal dispersion critically influence hydrogen activation and spillover, H_2-TPR measurements were further conducted to evaluate the reduction behavior and metal–support interactions of $3Ni/TiO_2$ catalysts with varying Ru loadings (0, 0.3, 0.7, and 1) in (Fig. 2a). The introduction of low to moderate Ru contents (Ru = 0.3–0.5) shifts the NiO reduction peaks to lower temperatures (≈250–330 °C) and increases peak intensity, indicating improved dispersion and facilitated hydrogen activation *via* Ru-induced spillover.[48] In addition, the H_2-TPR profiles exhibit four distinct reduction peaks, corresponding to Ru–Ni species with varying degrees of interaction with the TiO_2 support. In contrast, further increasing the Ru loading (Ru = 0.7–1) results in broader reduction features with a noticeable shift toward higher temperatures (>400 °C), characteristic of strengthened Ni–TiO_2 interactions associated with SMSI.[49]

The hydrogen adsorption–desorption properties of $3Ni/TiO_2$ catalysts with different Ru-to-Ni ratios were investigated by H_2-TPD (Fig. 2b). This analysis enables direct correlation between Ru loading, hydrogen storage capability, and catalytic performance in the hydrogen-buffer-assisted HDO process. H_2-TPD analysis reveals a strong dependence of hydrogen storage behavior on Ru loading in the Ni/TiO_2 catalysts. Monometallic of $3Ni/TiO_2$ and $0.7Ru/TiO_2$ exhibit negligible hydrogen desorption over the investigated temperature range of 3.92×10^{-3} mmol and 3.03×10^{-3} mmol (Table S1), indicating limited hydrogen uptake and poor reaction with hydrogen-buffer reaction. The $3Ni0.3Ru/TiO_2$ catalyst shows a distinct desorption feature in the intermediate-temperature region (≈250–500 °C), corresponding to chemisorbed hydrogen associated with well-dispersed metal sites and Ru-induced hydrogen spillover of capacity 2.70×10^{-2} mmol (Fig. S8 and Table S1) from moderate to strong adsorption. Further increasing the Ru content ($3Ni0.5Ru/TiO_2$ and $3Ni0.7Ru/TiO_2$) leads to broader desorption profiles and higher hydrogen uptake of 7.35×10^{-2} mmol and 7.33×10^{-2} mmol (Fig. S9, S10 and Table S1), indicating a wider distribution of adsorption sites with varying binding strengths (weak, moderate, and strong adsorption). Notably, $3Ni1Ru/TiO_2$ exhibits the strongest and highest-temperature hydrogen desorption (>600 °C) of uptake 4.56×10^{-2} mmol (Fig. S2 and Table S1), suggesting the presence of strongly bound hydrogen species stabilized at Ru–Ni–TiO_2 interfacial sites.[50–52] At higher temperatures (>700 °C), all samples showed only weak desorption features, confirming limited hydrogen spillover on TiO_2 supports.[53] This balance between adsorption and release is ideal for dynamic proton–electron transfer, supporting efficient H* shuttling by SiW_{12} rather than H accumulation on the catalyst surface.[29] These results indicate that Ru optimizes Ni–H binding strength, allowing efficient hydrogen exchange with the SiW_{12} buffer during aqueous-phase HDO.

To evaluate whether surface acidity contributes significantly to the hydrogen-buffer-assisted HDO performance, NH_3-TPD experiments were conducted, as shown in (Fig. 2c), and the corresponding acid site densities, obtained by integrating the desorption peaks, are summarized in (Table S2). The $0.7Ru/TiO_2$ catalyst exhibits the highest total acidity (0.544 mmol g^{-1}), with contributions from strong, moderate, and weak acid sites. In contrast, the bimetallic $3Ni0.7Ru/TiO_2$ catalyst shows a lower total acidity (0.237 mmol g^{-1}) than $0.7Ru/TiO_2$, but higher than monometallic $3Ni/TiO_2$ (0.177 mmol g^{-1}), which is dominated by moderate acid sites. Despite the higher acidity of $0.7Ru/TiO_2$, its inferior catalytic performance compared with $3Ni0.7Ru/TiO_2$ clearly suggests that high acidity alone does not correlate with enhanced HDO activity.[54] The results suggest that the superior performance of $3Ni0.7Ru/TiO_2$ is pri-

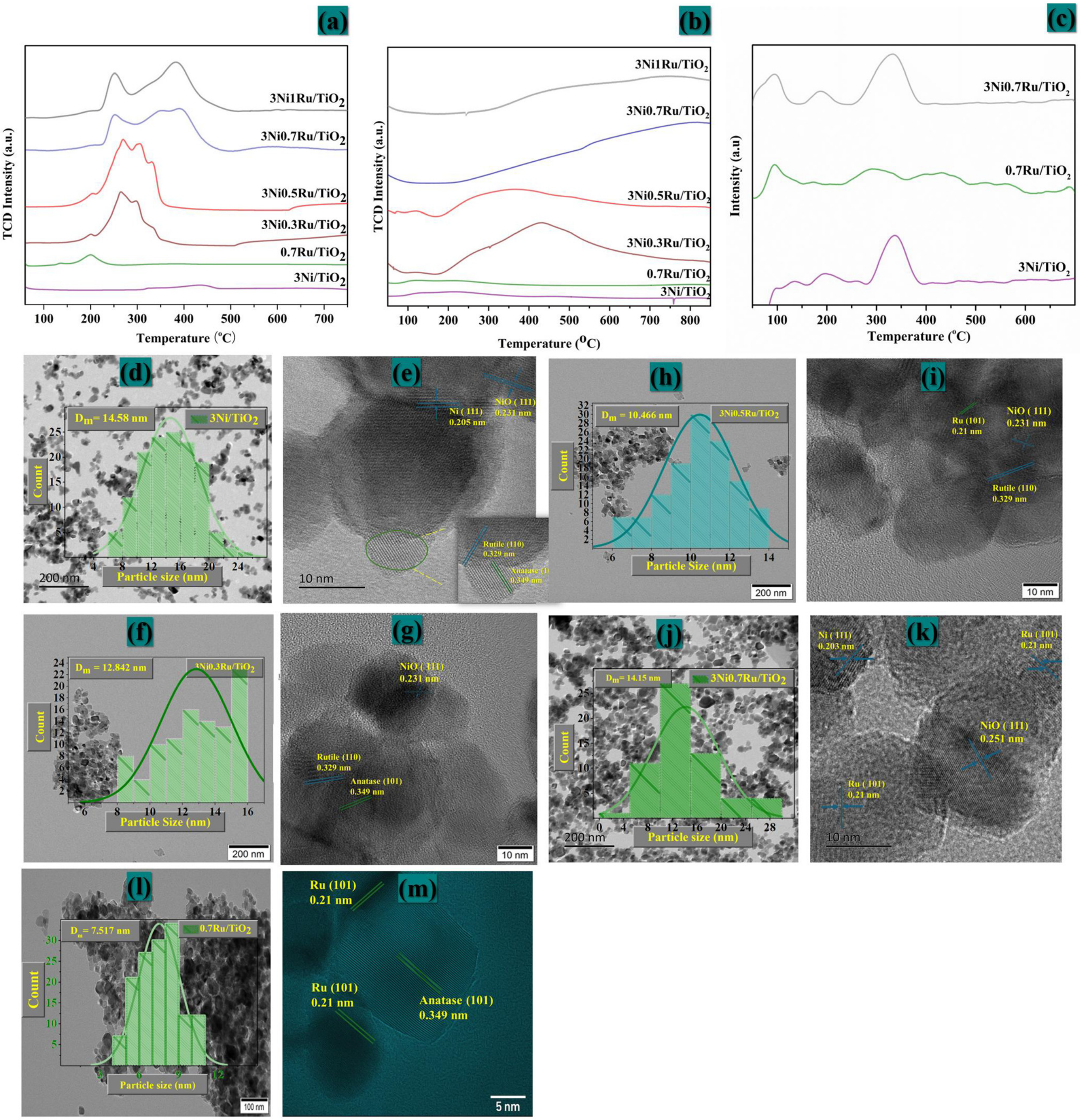

Fig. 2 Characterization of 3Ni/TiO$_2$ catalysts with varying Ru loadings prior to the HDO reaction. (a) H$_2$-TPR profiles, (b) H$_2$-TPD profiles, and (c) NH$_3$-TPD profiles. HRTEM images of the reduced catalysts showing the mean particle sizes of monometallic Ni and Ru, and bimetallic Ni–Ru on TiO$_2$: (d and e) 3Ni/TiO$_2$, (f and g) 3Ni0.3Ru/TiO$_2$, (h and i) 3Ni0.5Ru/TiO$_2$, (j and k) 3Ni0.7Ru/TiO$_2$, and (l and m) 0.7Ru/TiO$_2$ (catalyst reduction temperature: 450 °C under pure hydrogen (30 ml min^{-1}) for 2 h).

marily attributed to the synergistic combination of efficient hydrogen activation, hydrogen-transfer capability, and favorable metal–metal and metal–support interactions, which together promote effective coupling with the SiW$_{12}$ hydrogen-buffer system.

To understand how Ru loading influences metal dispersion and particle size in the 3Ni/TiO$_2$ system, HRTEM was used (Fig. 2). For the monometallic 3Ni/TiO$_2$ catalyst (Fig. 2d–e), clear lattice fringes with spacings of 0.349 and 0.329 nm were observed, corresponding to the (101) plane of anatase and the (110) plane of rutile, confirming that both TiO$_2$ phases are present in the P25 support.[55] Metallic Ni particles were identified by a *d*-spacing of 0.203 nm, assigned to the (111) plane of face-centered cubic Ni, together with a minor contribution from NiO (0.205 nm), in agreement with the H_2-TPR (Fig. 2a) and XRD results (Fig. S12).[36,56]

When Ru was introduced to form the bimetallic 3NixRu/TiO_2 catalysts (x = 0.3–1.0) (Fig. 2h–k), the metal particles became noticeably smaller, with the average size decreasing from 14.58 to 7.98 nm. This indicates that Ru effectively limits Ni particle growth and improves overall dispersion. HAADF-STEM images (Fig. S13) showed that Ni and Ru are generally well distributed across the TiO_2 surface, although small regions of agglomeration remain, likely because Ru preferentially nucleates on pre-existing Ni clusters. The lack of distinct Ru peaks in the XRD pattern of 3Ni0.7Ru/TiO_2 (Fig. S12), further suggests that Ru is present as highly dispersed or ultrafine nanoparticles below the detection limit, whereas the monometallic 0.7Ru/TiO_2 sample displays the highest apparent dispersion due to its low metal loading.

N_2 physisorption results (Fig. S14, S15 and Table S2) show that adding Ru leads to a slight decrease in surface area and pore volume compared to 3Ni/TiO_2 (from 49.65 to 49.37 m^2 g^{-1} and from 0.2873 to 0.2381 cm^3 g^{-1}, respectively), along with a reduction in average pore diameter (from 28.33 to 20.05 nm). These changes suggest that part of the Ru is deposited within the pore structure.

Afterwards, XPS was employed to probe to investigate the electronic structure and chemical valence states of the bimetallic 3Ni0.7Ru/TiO_2 catalyst and to compare them with those of the monometallic 3Ni/TiO_2 reference (Fig. 3). As shown in (Fig. 3a), the XPS survey spectrum of 3Ni0.7Ru/TiO_2 exhibits characteristic peaks corresponding to C 1s/Ru 3d (283.3 eV), Ru 3p (479.3 eV), O 1s (534.2 eV), Ni 2p (854.1 eV), and Ti 2s and Ti 2p at (568.1 eV) and (466.2 eV), respectively, confirming the presence of all constituent elements at the catalyst surface. High-resolution Ni 2p spectra for both 3Ni/TiO_2 and 3Ni0.7Ru/TiO_2 are presented in (Fig. 3b). For 3Ni0.7Ru/TiO_2, the Ni $2p_{3/2}$ and Ni $2p_{1/2}$ regions display two distinct components, with Ni $2p_{3/2}$ peaks located at (852.1 eV) and (858.2 eV) and Ni $2p_{1/2}$ peaks at (855.9 eV) and (861.1 eV). Pronounced satellite features at (856.0 eV) and (861.9 eV) are also observed, consistent with previous reports.[57] Compared with the monometallic 3Ni/TiO_2 catalyst, a systematic shift of the Ni 2p peaks toward higher binding energies is evident in the bimetallic sample, indicating electronic modification of Ni induced by the presence of Ru and the TiO_2 support. This shift points to partial electron withdrawal from Ni, consistent with stronger metal–metal and metal–support interactions that facilitate hydrogen spillover and enhance surface hydrogen mobility, in line with the H_2-TPR results. The resulting electronic asymmetry stabilizes higher-valent Ni species, while the comparatively electron-rich Ru sites help limit excessive oxidation of Ni. At the same time, these Ru sites favor balanced H_2 adsorption–desorption behavior, giving rise to a bifunctional enhancement of catalytic performance.[58–60] The Ru 3d spectrum of 3Ni0.7Ru/TiO_2 (Fig. 3c) reveals two pairs of peaks centered at (279.3 eV) and (280.1 eV), which are assigned to Ru^0 $3d_{5/2}$ and Ru^{4+} $3d_{5/2}$, respectively, indicating the coexistence of metallic and oxidized Ru species at the surface.[61] Such a mixed-valence Ru environment further substantiates that Ru serves as the primary hydrogen activation center in the bimetallic system.[62] The O 1s spectra (Fig. 3d) display a dominant lattice oxygen component at 529.9 eV and a higher binding energy contribution at approximately 531.4 eV, which corresponds to lattice oxygen and adsorbed oxygen.[63] Finally, the Ti 2p region (Fig. 3e) shows characteristic peaks at 458.7 eV (Ti $2p_{3/2}$) and 464.7 eV (Ti $2p_{1/2}$), confirming that the TiO_2 support retains its Ti^{4+} oxidation state after metal deposition and reduction.[64] Collectively, the XPS results indicate a synergistic catalytic architecture in which Ru predominantly functions as the active site for hydrogen activation through its metallic Ru^0 species, while Ni, electronically modified by both Ru and TiO_2, contributes to interfacial hydrogen transfer and activation of oxygenated surface intermediates.

3.2 Synergic hydrogen buffer effect and bimetallic catalysts

In this section, we investigated how coupling SiW_{12} with noble-metal-promoted 3Ni/TiO_2 catalysts affects the hydrogen-buffer cycle and its contribution to guaiacol HDO under mild conditions. To provide insight into the proposed hydrogen-transfer mechanism, electrode potential measurements were first performed to examine the intrinsic redox behavior and reversible hydrogen-transfer capability of SiW_{12} in aqueous media. Purging H_2 into a SiW_{12} solution caused a pronounced decrease in electrode potential, while subsequent purging with inert gas restored the potential to its original value (Fig. 4a). In the absence of a catalyst, no permanent color change or stable reduced species was observed, indicating that SiW_{12} does not directly react with molecular hydrogen at the gas–liquid interface. When 3Ni/TiO_2 was introduced, the potential decrease upon H_2 purging became significantly slower, and no stable blue coloration associated with reduced $[SiW_{12}]^{5-}$ species was detected (Fig. 4b). The observed blue coloration originates from reduction of SiW_{12} at the Pt electrode surface used during electrochemical measurements, rather than from catalytic reduction by Ni/TiO_2 itself.[28] These observations, together with the weak low-temperature hydrogen uptake observed in H_2-TPD (Fig. 1b), indicate that monometallic Ni struggles to activate and transfer hydrogen to SiW_{12} in water under ambient aqueous conditions, owing to the relative instability of nickel species in aqueous media, which leads to progressive catalyst deactivation.[65,66] In addition, surface passivation/limited interfacial contact in water may also contribute.[67,68]

In contrast, incorporation of noble metal promoters (Pt, Ru, or Pd) into 3Ni/TiO_2 dramatically altered the redox response of the SiW_{12} solution (Fig. 4c). Upon H_2 bubbling, the solution rapidly turned deep blue, accompanied by a sharp drop in electrode potential, consistent with the reduction of $[SiW_{12}]^{4-}$ to $[SiW_{12}]^{5-}$ (Fig. 4c).[21,28] The potential subsequently stabilized at a low value, indicating the establishment of a redox equilibrium in the presence of the catalyst. This behavior reflects catalytic dissociation of H_2 on the metal sites followed by transfer of hydrogen equivalents to SiW_{12}, forming a reversible hydrogen-buffering cycle described by eqn (3). Cyclic voltammetry (Fig. S16) confirms this mechanism by revealing a

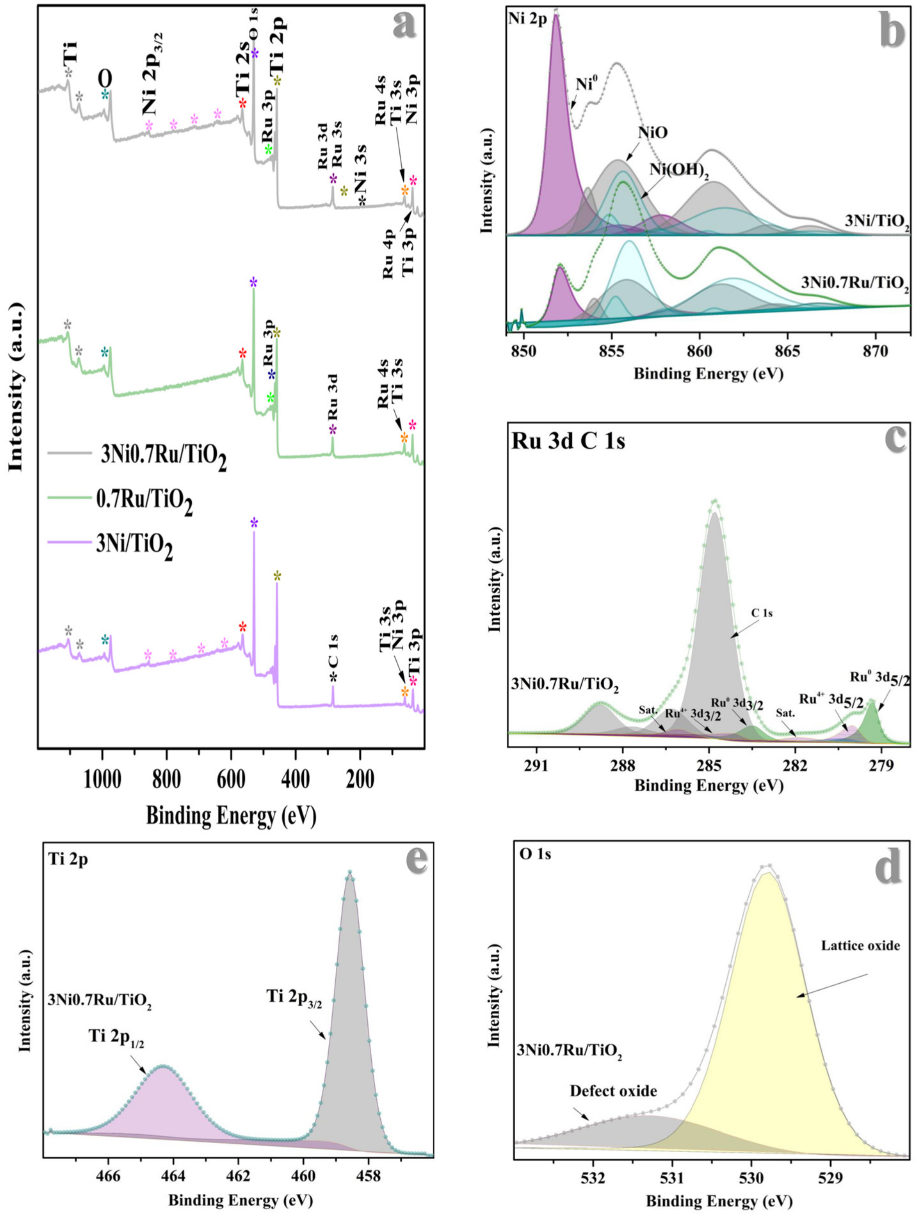

Fig. 3 High resolution XPS of $3Ni/TiO_2$ and $3Ni0.7Ru/TiO_2$ Catalysts prior to the HDO reaction: (a) Wide XPS Spectra, (b) Ni 2p, (c) Ru 3d and C 1s, (d) O 1s, and (e) Ti 2p (catalyst reduction temperature: 450 °C under pure hydrogen for 2 h).

reversible one-electron redox couple centered at approximately −0.15 V *versus* NHE, characteristic of the $[SiW_{12}]^{4-}/[SiW_{12}]^{5-}$ transition and consistent with previous reports.[21,28,30]

$$\frac{1}{2}H_2 + [SiW_{12}]^{4-} \rightleftharpoons H^{\bullet} + [SiW_{12}]^{4-} \rightleftharpoons H^{+}[SiW_{12}]^{5-} \quad \text{with NiRu catalyst.} \tag{3}$$

Under these conditions, an equilibrium is established among $[SiW_{12}]^{4-}$, $[SiW_{12}]^{5-}$, surface hydrogen species (H^*), protons (H^+), and molecular hydrogen (H_2). The reduced $[SiW_{12}]^{5-}$ species remains stable under an inert atmosphere unless both $[SiW_{12}]^{5-}$ and H^+ interact simultaneously at the catalyst surface, indicating that hydrogen release is surface-mediated.[21] Consequently, SiW_{12} serves as an efficient hydrogen carrier, enabling transfer of hydrogen from the gas–liquid interphase into the liquid phase through reversible proton–electron transfer and transfers reactive hydrogen into the bulk solution to regenerate H^* on the catalyst surface (reverse reaction).[28] The proposed hydrogen-buffering mechanism for the $3Ni1Ru/TiO_2$ with SiW_{12} system, which is also applicable to $3Ni1Pt/TiO_2$ and $3Ni1Pd/TiO_2$, is illustrated in (Fig. 5).

In order to further confirm the H state in SiW_{12} solution, the pH change was measured during H_2 reduction of SiW_{12} solution suspended with $3Ni1Ru/TiO_2$, a gradual decline in pH was observed, attributed to H_2 was oxidized by $[SiW_{12}]^{4-}$ to be

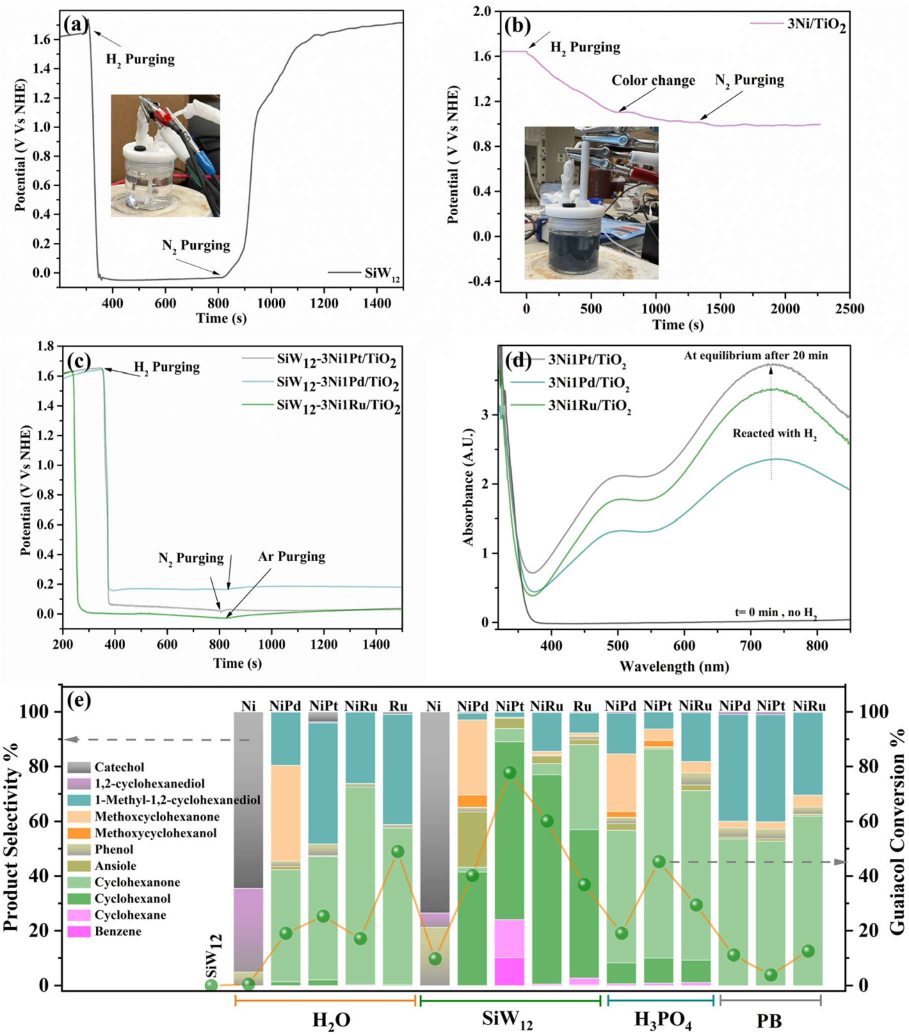

Fig. 4 Comparison of electrode potential changes during H_2 purging in monometallic and bimetallic catalysts within SiW_{12}-based catalytic systems: (a) SiW_{12} without catalyst, (b) 3Ni/TiO_2, and (c) bimetallic catalysts supported on TiO_2 (SiW_{12} = 0.012 mol L^{-1}, catalyst = 0.08 g). (d) UV–Vis absorbance intensities of SiW_{12}-based catalysts (Ni–Pt, Ni–Ru, and Ni–Pd) following the potential change test. (e) Comparison of guaiacol HDO performance and product selectivity in phosphate buffer (PB, pH = 7), H_3PO_4, and SiW_{12} catalytic systems (reaction conditions: 95 °C, 1 MPa H_2, 9 mL water, 0.08 g catalyst, 0.05 mol L^{-1} SiW_{12}, 1 mL guaiacol, and 1 h reaction time).

free proton H^+ in bulk solution, and simultaneously the electron was stored in the $[SiW_{12}]^{5-}$ anions (Fig. S17). This trend indicates efficient transport of electrons and protons from the gas–liquid boundary into the bulk of the solution, similarly to our previous research.[28,30]

Electrode potential measurements revealed clear differences in the degree of SiW_{12} reduction (Fig. 4c). The potentials stabilized at approximately +0.01 V for both 3Ni1Ru/TiO_2 and 3Ni1Pt/TiO_2, whereas 3Ni1Pd/TiO_2 reached a significantly higher value of +0.20 V, indicating a markedly lower extent of acid reduction (Fig. 4c). Because lower electrode potentials correspond to deeper reduction of $[SiW_{12}]^{4-}$ to $[SiW_{12}]^{5-}$, these results suggest that Ru- and Pt-promoted catalysts facilitate substantially greater hydrogen transfer to SiW_{12} than the Pd-containing system.[69] Spectroscopic analyses further corroborated this trend. UV–Vis spectra recorded after 20 min of H_2 bubbling (Fig. 4d) exhibited the highest absorbance intensities for 3Ni1Ru/TiO_2 and 3Ni1Pt/TiO_2, corresponding to higher concentrations of reduced $[SiW_{12}]^{5-}$ species, consistent with more effective hydrogen transfer and metal–acid interaction.[30] Visual inspection likewise showed a deep blue coloration for the Ru- and Pt-promoted systems, whereas only a faint color change was observed for 3Ni1Pd/TiO_2 (Fig. S18), confirming its limited reduction capability. Together, these observations indicate that 3Ni1Ru/TiO_2 and 3Ni1Pt/TiO_2 establish comparable hydrogen transfer within the SiW_{12}-mediated system.

Despite exhibiting a similar overall reduction extent of $[SiW_{12}]^{4-}$ to $[SiW_{12}]^{5-}$, the catalysts displayed distinct hydrogen-transfer kinetics. The Pt-promoted catalyst reached a stable reduced state within approximately 10 min, whereas the Ru-promoted catalyst required about 15 min to achieve a similar reduction state (Fig. 4c). H_2-TPD measurements

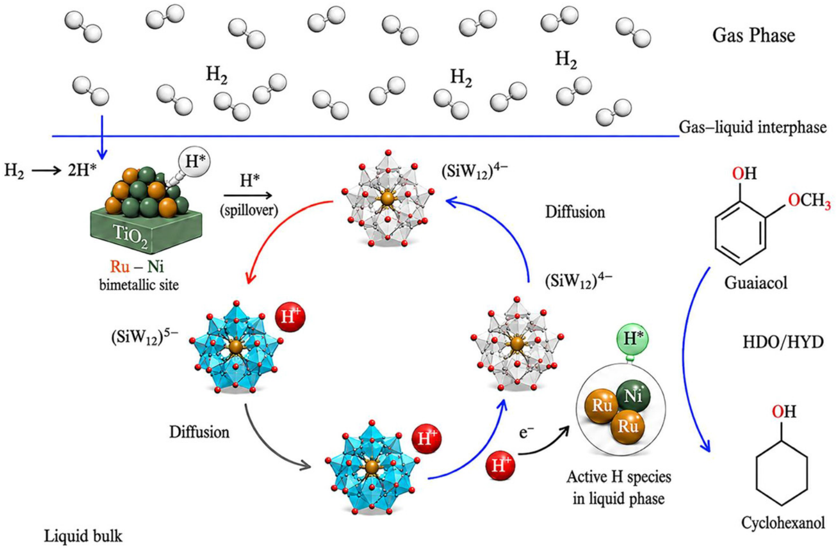

Fig. 5 Proposed mechanism of bimetallic ($NiRu/TiO_2$) with SiW_{12} at ambient reaction conditions (adopted from *Liu et al.*[21]) for HDO of guaiacol.

(Fig. 1b) provide insight into this difference. $3Ni1Pt/TiO_2$ displayed a higher density of weakly adsorbed hydrogen species, particularly below 100 °C (Fig. 1b and Table S1), which facilitates rapid formation and migration of reactive H* species. In contrast, $3Ni1Ru/TiO_2$ exhibited lower overall hydrogen uptake at low temperature, consistent with slightly stronger hydrogen binding that slows equilibration but maintains effective hydrogen delivery.[70,71] By comparison, $3Ni1Pd/TiO_2$ showed the lowest total hydrogen uptake, despite the presence of both weak and strong adsorption sites, explaining its inferior ability to sustain the SiW_{12} hydrogen-buffering cycle. Accordingly, the overall hydrogen-buffer-assisted catalytic activity followed the order: $3Ni1Pt/TiO_2$ > $3Ni1Ru/TiO_2$ > $3Ni1Pd/TiO_2$. H_2-TPR results (Fig. 1a) further suggest that metal–support interactions weaken in the order $3Ni1Pd/TiO_2$ > $3Ni1Ru/TiO_2$ > $3Ni1Pt/TiO_2$. Stronger metal–support coupling can restrict hydrogen mobility and interfacial hydrogen transfer to SiW_{12}, thereby limiting effective hydrogen spillover.[72] These observations also follow the well-known volcano relationship between hydrogen adsorption energy and catalytic activity. Metals that bind hydrogen either too strongly or too weakly lie on either side of the activity maximum and therefore exhibit lower reactivity.[28] The moderate hydrogen adsorption strength of Pt favors the generation of mobile, reactive H* species capable of efficiently reducing SiW_{12}, while the stronger hydrogen binding on Ni-, Pd-, and Ru-containing surfaces stabilizes surface hydrogen, slowing hydrogen spillover and limiting SiW_{12}-mediated buffering under mild multiphase reaction conditions.[73]

The impact of this hydrogen-buffering mechanism was directly reflected in guaiacol HDO performance as shown in (Fig. 4e). To decouple the specific role of SiW_{12} from that of Brønsted acidity alone, control experiments were conducted in pure water, phosphate buffer (PB, pH 7) and in H_3PO_4 solution (pH 2.1, 0.05 mol L^{-1}) as reference acid promoters (Fig. 4e). In pure water, all catalysts exhibited low guaiacol conversion and predominantly formed partially oxygenated products such as catechol, phenol, and 1-methyl-1,2-cyclohexanediol, indicating that although Ni, Pt, Pd and Ru can dissociate/activate H_2, the aqueous environment strongly stabilizes oxygenated intermediates through hydrogen bonding and solvation effects and increases the energetic barrier for deep hydrogenation and C–O bond cleavage. At the same time, surface hydrogen generated on metal sites becomes partially immobilized within the hydrogen-bonding network of water, lowering the effective surface hydrogen chemical potential required for C–O bond cleavage and complete hydrogenation.[74,75] Previous studies have shown that guaiacol undergoes transalkylation followed by rapid aromatic ring hydrogenation to form this diol over Ni-based catalysts.[76] Introducing PB further dropped, guaiacol conversion below 12% for all catalysts, demonstrating that neutral acidity cannot couple hydrogen activation with efficient hydrogen transfer to the substrate. Even when H_3PO_4 was introduced, only a modest increase in conversion was achieved, and product distributions remained dominated by cyclohexanone around 70% selectivity over $3Ni1Pt/TiO_2$ and $3Ni1Ru/TiO_2$. This behavior is consistent with enhanced HDO activity facilitated by altered hydrogen adsorption properties in the presence of hydronium ions,[21] but the persistence of cyclohexanone and the near absence of cyclohexanol indicate that hydrogen delivery to carbonyl intermediates remains kinetically limited.[77] In sharp contrast, incorporation of SiW_{12} led to a simultaneous and substantial enhancement in both guaiacol conversion and cyclohexanol selectivity across all catalysts, despite SiW_{12} itself being inactive toward guaiacol HDO, as neutral phenol cannot readily form the high-energy phenoxide intermediate required for subsequent hydrogenation steps.[78] In the presence of both SiW_{12} and metal catalysts, guaiacol conversions reached 40.2%, 77.7%, and 60.2% over $3Ni1Pd/TiO_2$, $3Ni1Pt/TiO_2$, and $3Ni1Ru/TiO_2$, respectively, with corresponding cyclohexanol selectivity's of 41.5%, 65.1%, and 76.5%. These results, compared with H_3PO_4, clearly suggest that SiW_{12} functions as an effective hydrogen buffer, coupling metal-catalyzed H_2 activation with hydrogen transfer through reversible H^+/e^- exchange. In this role, SiW_{12} acts as a proton-responsive redox mediator that stores and transfers reactive hydrogen equivalents at the catalyst interface, promoting hydrogenation and C–O bond cleavage under under mild multiphase reaction conditions.[21] The lower activity of the Pd-promoted catalyst is consistent with literature reports showing that Pd-based systems require substantially higher temperatures and hydrogen pressures to achieve efficient demethoxylation and carbonyl hydrogenation.[79,80] Limited hydrogenation of polar intermediates leads to ketone accumulation, suppressing deep HDO under mild condition,[81] whereas Pt- and Ru-based catalysts more readily hydrogenate and deoxygenate such species in the presence of Brønsted acids.[77] Although 3Ni1Pt/TiO_2 exhibited the highest initial guaiacol conversion, 3Ni1Ru/TiO_2 delivered significantly higher cyclohexanol selectivity, the proposed reaction pathways are illustrated in (Fig. S19a). Extending the reaction time over 3Ni1Ru/TiO_2 to 4 h increased guaiacol conversion above 80% (Fig. S19b), indicating that its lower initial activity reflects slower hydrogenation kinetics rather than intrinsic catalytic limitations. Furthermore, dehydroxylation of cyclohexanol over Ru surfaces can be kinetically slow, even under acidic conditions, which favors high cyclohexanol selectivity.[82] The observed differences in product distribution among Ni–Pt, Ni–Pd, and Ni–Ru catalysts can be further rationalized by considering the adsorption mode of guaiacol and the nature of hydrogen species involved. Guaiacol can adsorb either through the aromatic ring or *via* the oxygenated functional groups (–OH, $-OCH_3$) on metal sites. Ring adsorption typically facilitates hydrogenation pathways leading to cyclohexanone and cyclohexanol, whereas adsorption through oxygen functionalities promotes C–O bond activation and deoxygenation pathways.[83–86] This behavior is also consistent with differences in the interaction with SiW_{12}, reduction behavior, availability of hydrogen adsorption sites, average particle size, and metal–support interactions as discussed earlier. Based on its high cyclohexanol selectivity and strong C=O hydrogenation capability, the 3Ni1Ru/TiO_2 with SiW_{12} system was therefore identified as the preferred catalytic formulation for selective guaiacol HDO. In (Fig. 4e), further illustrates the distinct yet complementary roles of Ni, Ru, and the Ni–Ru interface in guaiacol HDO within the SiW_{12}-assisted system. In water, 3Ni/TiO_2 is essentially inactive, whereas 1Ru/TiO_2 exhibits higher conversion and predominantly forms cyclohexanone, reflecting Ru's strong ability to hydrogenate aromatic rings and oxygen-containing functional groups. The bimetallic 3Ni1Ru/TiO_2 displays intermediate behavior between these two cases. The relatively higher activity of 1Ru/TiO_2 may also be partially associated with its higher total acidity, as revealed by the NH_3-TPD results, compared with 3Ni1Ru/TiO_2 in (Fig. 2c). Upon addition of SiW_{12}, the most pronounced enhancement is observed for 3Ni1Ru/TiO_2, which achieves the highest guaiacol conversion and more than 70% cyclohexanol selectivity, whereas 1Ru/TiO_2 exhibits only a limited response. This trend is consistent with previous reports showing that Ru catalysts in acidic aqueous environments tend to favor rearrangement and isomerization pathways rather than direct HDO, often resulting in lower phenol conversion.[77] Electrochemical and hydrogen adsorption measurements support this interpretation. Although 1Ru/TiO_2 exhibits a significant potential decrease upon H_2 purging, indicating effective H_2 activation, only a limited potential recovery is observed during Ar purging (Fig. S20), indicating less dynamic reversible hydrogen exchange within the SiW_{12}-mediated hydrogen-buffer system compared with 3Ni1Ru/TiO_2. Similarly, H_2-TPD results (Fig. 2b) suggest that hydrogen on 1Ru/TiO_2 is less involved in transferable surface hydrogen species than on 3Ni1Ru/TiO_2. Although Ru is highly active for H_2 dissociation, the relatively strong Ru–H interaction can slow hydrogen desorption and reduce hydrogen mobility on the catalyst surface, thereby limiting effective coupling with the SiW_{12} hydrogen-buffer cycle.[87] Consequently, hydrogen on 1Ru/TiO_2 interacts less effectively with the SiW_{12}-mediated hydrogen-transfer process. Therefore, the superior performance of 3Ni1Ru/TiO_2 is attributed to the synergistic interaction between Ni and Ru, which enhances hydrogen mobility and interfacial hydrogen-transfer processes, leading to more efficient utilization of the SiW_{12} hydrogen-buffer system during HDO.

3.3 Synergistic metal–acid interactions

To understand the interaction between SiW_{12} and 3Ni1Ru/TiO_2 during guaiacol HDO, we combined structural characterization, H_2-TPD analysis, *in situ* DRIFTS, XRD, Raman, O_2-TPO and catalytic evaluation (Fig. 6). Post-reaction elemental mapping reveals uniform co-distribution of Si with Ni and Ru across the TiO_2 surface (Fig. 6a). Similar results obtained for 3Ni/TiO_2, 3Ni1Pt/TiO_2 and 3Ni1Pd/TiO_2 as shown in (Fig. S21 and S22). Repeated washing does not completely remove SiW_{12}, indicating that part of the initially soluble heteropoly acid becomes strongly associated with the catalyst surface under reaction conditions. XRD and Raman analyses (Fig. S23 and S24a) further support this observation, showing that the 3Ni1Ru/TiO_2 structure remains largely unchanged after reaction, while weak low-angle XRD features (5–10°) together with a slight reduction in Raman intensity suggests the presence of surface-associated SiW_{12} species.[88] This behavior is consistent with the adsorption of heteropoly species at metal–support interfaces, suggesting that SiW_{12} evolves from a homogeneous hydrogen buffer into an interfacial promoter during HDO.[88]

Two spatial configurations are therefore possible: (i) SiW_{12} anchored on TiO_2 in proximity to Ni–Ru sites (3Ni0.7Ru/SiW_{12}–TiO_2), and (ii) SiW_{12} partially coordinated on Ni–Ru nanoparticles (SiW_{12}@3Ni0.7Ru/TiO_2) as shown in (Fig. 6c). To decouple the influence of spatial arrangement, these two architectures were intentionally synthesized as control catalysts (SI section S2). This strategy enables direct assessment of how SiW_{12} location governs hydrogen adsorption, spillover dynamics, and catalytic activity.

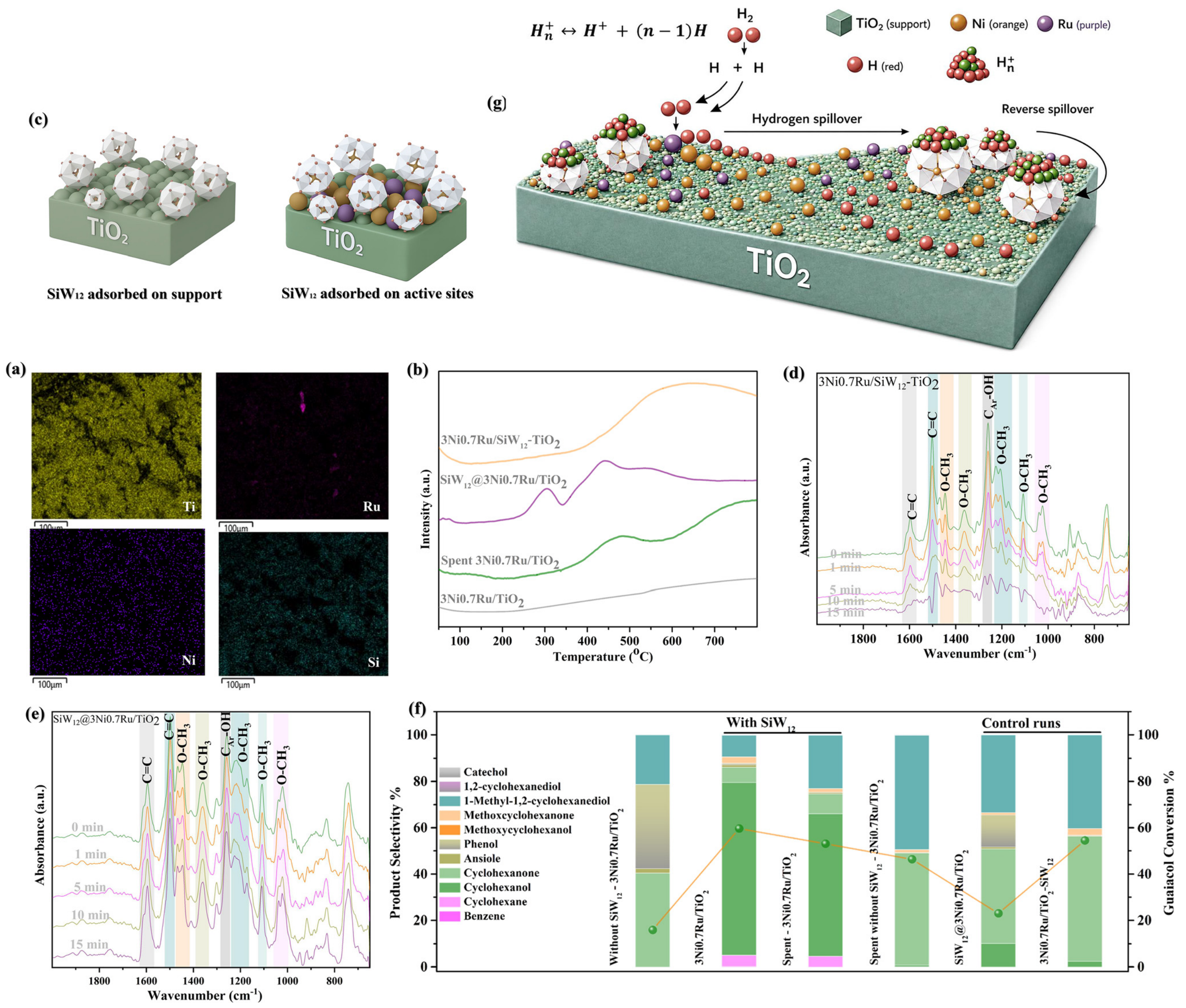

Fig. 6 (a) EDS elemental mapping of the spent 3Ni0.7Ru/TiO_2 catalyst after the HDO reaction. (b) H_2-TPD profiles collected after H_2 saturation at 50 °C for 45 min for fresh and spent 3Ni0.7Ru/TiO_2, SiW_{12}@3Ni0.7Ru/TiO_2 (SiW_{12} adsorbed on metal sites), and 3Ni0.7Ru/SiW_{12}–TiO_2 (SiW_{12} pre-adsorbed on the support). (c) Schematic illustration of the possible interactions between SiW_{12} and the catalyst surface. (d and e) *In situ* DRIFTS spectra of guaiacol adsorption under H_2 at 100 °C for 15 min over 3Ni0.7Ru/SiW_{12}–TiO_2 and SiW_{12}@3Ni0.7Ru/TiO_2, respectively. (f) Catalytic activity of the fresh catalyst spent catalyst and control catalysts under optimum reaction conditions. (g) Proposed spillover mechanism (reaction conditions: 125 °C, 0.5 MPa H_2, 9 mL water, 0.12 g catalyst, 0.025 mol L^{-1} SiW_{12}, 0.5 mL guaiacol, and 1 h reaction time).

H_2-TPD analysis provides insight into how this spatial distribution affects hydrogen activation and mobility (Fig. 6b). Fresh 3Ni0.7Ru/TiO_2 exhibits a broad desorption peak centered at around 350 °C, characteristic of moderately bound hydrogen arising from Ni–Ru electronic synergy.[36] After reaction with SiW_{12}, new low-temperature features (<150 °C) appear, indicating the formation of more weakly bound and mobile hydrogen species.[89] Enhanced desorption in the 300–450 °C range reflects hydrogen stabilized at metal–SiW_{12} interfacial sites, while a broad band above 500 °C evidences promoted hydrogen spillover onto TiO_2.[90] Control catalysts confirm this interpretation: direct coating of SiW_{12} on Ni–Ru (SiW_{12}@3Ni0.7Ru/TiO_2) generates strong interfacial hydrogen states, whereas support-anchored SiW_{12} (3Ni0.7Ru/SiW_{12}–TiO_2), primarily enhances hydrogen spillover and hydrogen distribution across the catalyst surface as shown in (Fig. 6b). These results suggest that SiW_{12} is not only anchored on the TiO_2 support but can also partially coat Ni–Ru nanoparticles, modifying hydrogen adsorption behavior depending on its location.

In situ DRIFTS further suggests the influence on guaiacol transformation (Fig. 6d–e) and (Fig. S25a and b). Characteristic C–H (2700–3000 cm^{-1}), aromatic C=C (1600–1490 cm^{-1}), and methoxy/O–H bands (1450–1000 and 3400–3600 cm^{-1}) gradually decrease with time-on-stream, accompanied by the growth of aliphatic features, indicating progressive hydrogenation.[91] Notably, 3Ni0.7Ru/SiW_{12}–TiO_2 exhibits faster attenuation of aromatic bands and stronger aliphatic signal development compared to SiW_{12}@3Ni0.7Ru/TiO_2 and bare 3Ni0.7Ru/TiO_2 (Fig. S25), confirming that support-anchored SiW_{12} accelerates hydrogenation, consistent with the H_2-TPD results in (Fig. 6b). In addition, O_2-TPO analysis (Fig. S24b) revealed substantially lower carbonaceous deposition in the presence of dissolved SiW_{12} than in the water-only system, suggesting that enhanced hydrogen transfer suppresses the condensation and polymerization of oxygenated intermediates.[88]

These structural and spectroscopic observations correlate well with the catalytic performance shown in (Fig. 6f). The spent catalyst retains considerable activity even without SiW_{12} in solution during the second reaction cycle, maintaining approximately 45% guaiacol conversion. In contrast, bare 3Ni0.7Ru/TiO_2 achieves only about 15% conversion. This sustained performance further indicates that a portion of SiW_{12} remains strongly associated with the catalyst surface and continues to participate in the hydrogen-buffer cycle. Interestingly, when fresh SiW_{12} is reintroduced to the spent catalyst, a slight decrease in activity is observed. This suggests that excessive SiW_{12} deposition may partially block Ni–Ru active sites required for H_2 dissociation. The control experiments further support this interpretation, demonstrating that optimal catalytic performance depends on the spatial distribution of SiW_{12} rather than simply its presence. Where direct deposition of SiW_{12} onto Ni–Ru nanoparticles suppresses activity due to excessive surface coverage blocks metal sites required for H_2 dissociation. In contrast, when SiW_{12} is predominantly anchored on the TiO_2 support near the metal sites, conversion increases to approximately 50%, as supported by the H_2-TPD (Fig. 6b) and *in situ* DRIFTS results (Fig. 6d–e).

This architecture-dependent behavior is rationalized by a non-classical bifunctional hydrogen spillover mechanism at the metal–acid interface as seen in (Fig. 6g).[92] Hydrogen molecules first split on the metallic Ni–Ru surface, forming reactive hydrogen species. These hydrogen atoms can then move from the metal surface to nearby SiW_{12} acid sites. When they reach the acid sites, they interact with the protons already present on SiW_{12}, forming hydrogen species that are more stable but still reactive. At the same time, this process is not one-directional. As hydrogen accumulates on the SiW_{12} surface, some of these reactive species can migrate back to the metallic Ni–Ru sites. In this way, a dynamic balance is established between hydrogen on the metal and hydrogen on the acid phase. This continuous exchange creates a layer of reactive hydrogen species distributed across the catalyst surface. Similar to previously reported systems, the strong interaction between SiW_{12} and Ru-containing sites likely facilitates hydrogen exchange between the metal surface and the heteropoly species.[93] In this way, SiW_{12} functions not only as a Brønsted acid but also as a proton-responsive redox mediator that stores and transfers hydrogen equivalents at the catalyst interface.[21] The close proximity between the metal and acid phases promotes dynamic hydrogen exchange across the catalyst surface, facilitating hydrogenation and HDO reactions without relying solely on surface-bound hydrogen species. Simultaneously, SiW_{12} protonates oxygenated phenolic intermediates to form oxonium species ($\Delta E_r \approx 22.1$ kJ mol^{-1}), which undergo facile dehydration to carbocation intermediates followed by hydrogenation to cyclohexanol (apparent activation energy ≈ 97.5 kJ mol^{-1}).[21,28,30] These results collectively suggest that the enhanced HDO performance arises from the cooperative interaction between the SiW_{12} hydrogen-buffer cycle in solution and the interfacial metal–acid interactions on the catalyst surface. Together, these processes establish a dynamic hydrogen-transfer network that facilitates hydrogen transport between the gas phase, liquid phase, and catalyst interface during HDO.

3.4 Process optimization and reaction parameters

Optimizing catalytic efficiency in heterogeneous reactions requires a clear understanding of how conditions like temperature, pressure, catalyst loading, and reactant loading influence product outcomes. In this study, the most active Ru-promoted 3Ni/TiO_2 catalyst was chosen to explore how these variables govern guaiacol HDO and its conversion pathway toward cyclohexanol.

3.4.1 Effect of metal loading. The combination of SiW_{12} with bimetallic 3NiRu/TiO_2 establishes a synergistic bifunctional system that enhances hydrogen transfer and HDO efficiency. To optimize this interaction, a series of Ru loadings (0, 0.3, 0.5, 0.7, and 1 wt%) was incorporated into 3Ni/TiO_2 (Fig. 7). Electrode potential measurements were used to probe catalyst–buffer interactions and to establish their correlation with HDO activity in the presence of SiW_{12} (Fig. S26). Upon H_2 purging, all samples exhibited a decrease in potential and a characteristic blue coloration (Fig. S27) indicating reduction of SiW_{12} and effective hydrogen uptake.[28] The stabilized potentials were −0.05 V for 3Ni1Ru/TiO_2 and 3Ni0.7Ru/TiO_2, −0.08 V for 3Ni0.5Ru/TiO_2, and −0.092 V for 3Ni0.3Ru/TiO_2, reflecting progressively weaker hydrogen transfer with decreasing Ru content. UV–Vis spectra (Fig. S26b) showed the highest absorbance intensities for 3Ni0.7Ru/TiO_2 and 3Ni1Ru/TiO_2, confirming greater formation of reduced $[SiW_{12}]^{5-}$ species. Accordingly, these results suggest that the effectiveness of the SiW_{12}-mediated hydrogen-buffer cycle followed the order: 3Ni1Ru/TiO_2 ≈ 3Ni0.7Ru/TiO_2 > 3Ni0.5Ru/TiO_2 > 3Ni0.3Ru/TiO_2. This trend correlates with differences in hydrogen adsorption capacity, metal dispersion, and accessibility of Ni^0–Ru^0 interfacial active sites, as discussed in the characterization section.

The impact of Ru loading on HDO performance is shown in (Fig. 7a). Increasing the Ru content from 0 to 0.5 wt% enhanced guaiacol conversion from 26.2% to 38.9% and improved selectivity toward deoxygenated products. Further increases to 0.7 and 1 wt% resulted in comparable conversion, indicating a saturation effect beyond 0.5 wt%. Notably, this trend is fully consistent with the SiW_{12} redox and hydrogen-buffering measurements, which showed the highest degree of $[SiW_{12}]^{4-}$ reduction and hydrogen uptake for 3Ni0.7Ru/TiO_2

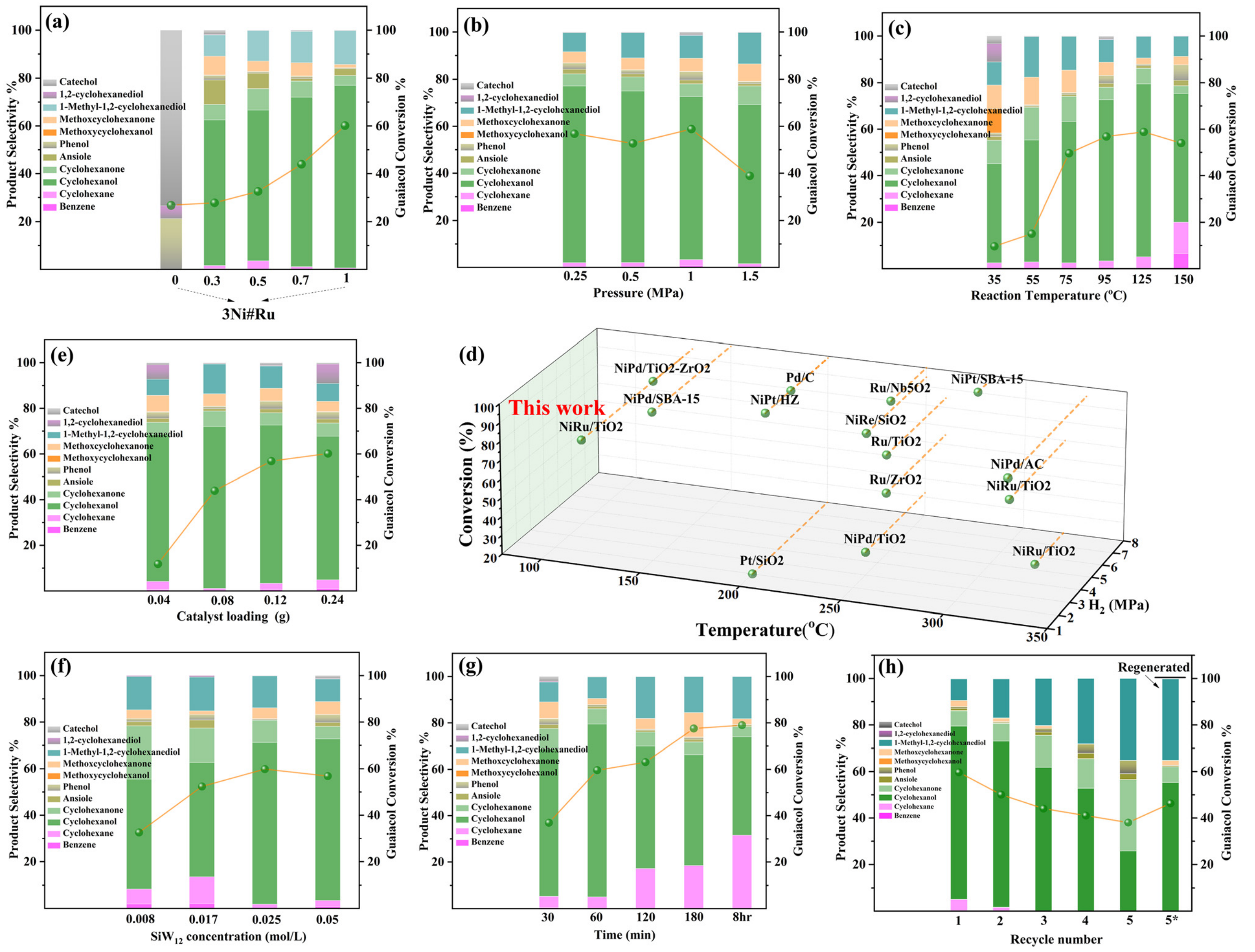

Fig. 7 (a) Comparison of catalytic activity for HDO conversion and product selectivity across different Ru loadings (0–1 wt%) on 3Ni/TiO_2 in SiW_{12}-assisted catalytic systems (reaction conditions: 95 °C, 1 MPa H_2, 9 mL water, 0.08 g catalyst, 0.05 mol L^{-1} SiW_{12}, 1 mL guaiacol, and 1 h reaction time). Effect of (b) hydrogen pressure (MPa), (c) reaction temperature (°C), (d) comparison with other catalysts reported for HDO of lignin derived bio-oil model compounds (Table S3), 5Ni1Pt/SBA-15,[110] Ni–Re/SiO_2,[111] NiRu/TiO_2,[36] NiRu/TiO_2,[112] PdNi/SBA-15,[113] NiPd/TiO_2,[44] NiPd/TiO_2–ZrO_2,[114] NiPt/SBA-15,[115] NiPd/AC,[116] NiPt/SBA-15,[117] NiPt/HZ,[118] NiRu/TiO_2,[119] Pd/C,[120] Ru/TiO_2,[121] Ru/Nb_2O_5,[122] Pt/SiO_2,[123] Ru/ZrO_2.[121] (e) Catalyst amount (g), (f) SiW_{12} concentration (mol L^{-1}) (reaction conditions: 95 °C, 1 MPa H_2, 9 mL water, 0.08 g catalyst, 0.05 mol L^{-1} SiW_{12}, 1 mL guaiacol, and 1 h reaction time). (g) Reaction time on the conversion of guaiacol and product selectivity and (h) recyclability and stability of 3Ni0.7Ru/TiO_2 (reaction conditions: 125 °C, 0.5 MPa H_2, 9 mL water, 0.12 g catalyst, 0.025 mol L^{-1} SiW_{12}, 0.5 mL guaiacol, and 1 h reaction time).

and 3Ni1Ru/TiO_2. Although both catalysts exhibited high activity and stability, 3Ni0.7Ru/TiO_2 provided the optimal balance between catalytic performance and noble metal utilization (Fig. S26c).

It's good to note that argon gas was used as the purge gas as the purge gas during the electrochemical measurements to evaluate the reversibility of the SiW_{12} redox cycle (Fig. S28 and Fig. 4c) to avoidcompetitive adsorption, as Ru exhibits a strong affinity for N_2 in the presence of H_2 and SiW_{12}.[28] Under H_2 purging, the electrode potential decreased and reached equilibrium within ~800 s, whereas subsequent introduction of N_2 caused a sharp potential increase with the highest increase recorded at a 3 : 1 N_2 : H_2 ratio, confirming competitive adsorption at the catalyst surface (Fig. S28b). This destabilized the SiW_{12} hydrogen-buffering cycle, leading to transient reduction of $[SiW_{12}]^{5-}$ (Fig. S28) and markedly lower guaiacol conversion (4.79–17.2%) with a shift toward cyclohexanone (62.95–67.14%) (Fig. S28a).[28]

3.4.2 Effect of temperature and pressure. Before initiating the optimization studies, it was essential to eliminate the effects of external diffusion to ensure a reliable investigation of the reaction pathway.[94] As shown in (Fig. S29), varying the stirring rate influenced the catalytic performance. Higher stirring rates enhanced the hydrogenation efficiency toward cyclohexanol by minimizing mass transfer limitations associated with the triphasic catalytic system (water–oil–solid), which involves two distinct hydrophobic layers. Based on these observations, a stirring rate of 1000 rpm was selected to effectively eliminate external diffusion effects and ensure uniform mixing.

The HDO of guaiacol under mild hydrogen pressure was examined to evaluate the influence of hydrogen pressure on guaiacol conversion and product selectivity. As shown in (Fig. 7b), increasing the hydrogen pressure from 0.25 to 1.0 MPa at 95 °C produced only a minor change in guaiacol conversion. Since guaiacol HDO in the SiW_{12}-assisted system proceeds predominantly through liquid-phase hydrogen transfer, the reaction is not solely governed by the availability of gaseous H_2.[21] Instead, the catalytic performance depends on the efficient transfer of reactive hydrogen equivalents through the SiW_{12} hydrogen-buffer cycle and their delivery to the catalyst interface. Consequently, increasing the inlet H_2 pressure beyond a certain level does not significantly enhance the reaction rate. The slight decrease in conversion observed at higher pressures at 1.5 MPa H_2, may be attributed to increased surface coverage of adsorbed hydrogen on the $3Ni0.7Ru/TiO_2$ catalyst, which can partially limit the availability of active metal–acid interfacial sites and disturb the balance between hydrogen activation, substrate adsorption, and interfacial hydrogen-transfer processes.[95] Moreover, the product distribution remained largely unchanged across the investigated pressure range, suggesting that hydrogenation *via* the dominant reaction pathway (Route 1, Fig. 8b) governs the reaction.[96] Based on these results, 0.5 MPa H_2 was selected as the optimal operating pressure.

Temperature optimization in HDO is critical, as it governs C–O bond cleavage efficiency, product selectivity, and the extent of secondary reactions and catalyst deactivation.[97] (Fig. 7c) illustrates the effect of temperature on guaiacol conversion and product distribution over the $3Ni0.7Ru/TiO_2$ catalyst in the presence of SiW_{12}. At 35 °C, the reaction proceeds under mild conditions, resulting in limited guaiacol conversion. As the temperature increases, both conversion and selectivity toward hydrogenated products (cyclohexanol and cyclohexane) improve, while the formation of intermediate species such as phenol and 1-methyl-1,2-cyclohexanediol decreases. Further increasing the temperature to 150 °C leads to a slight decline in conversion 54.28% and a reduction in

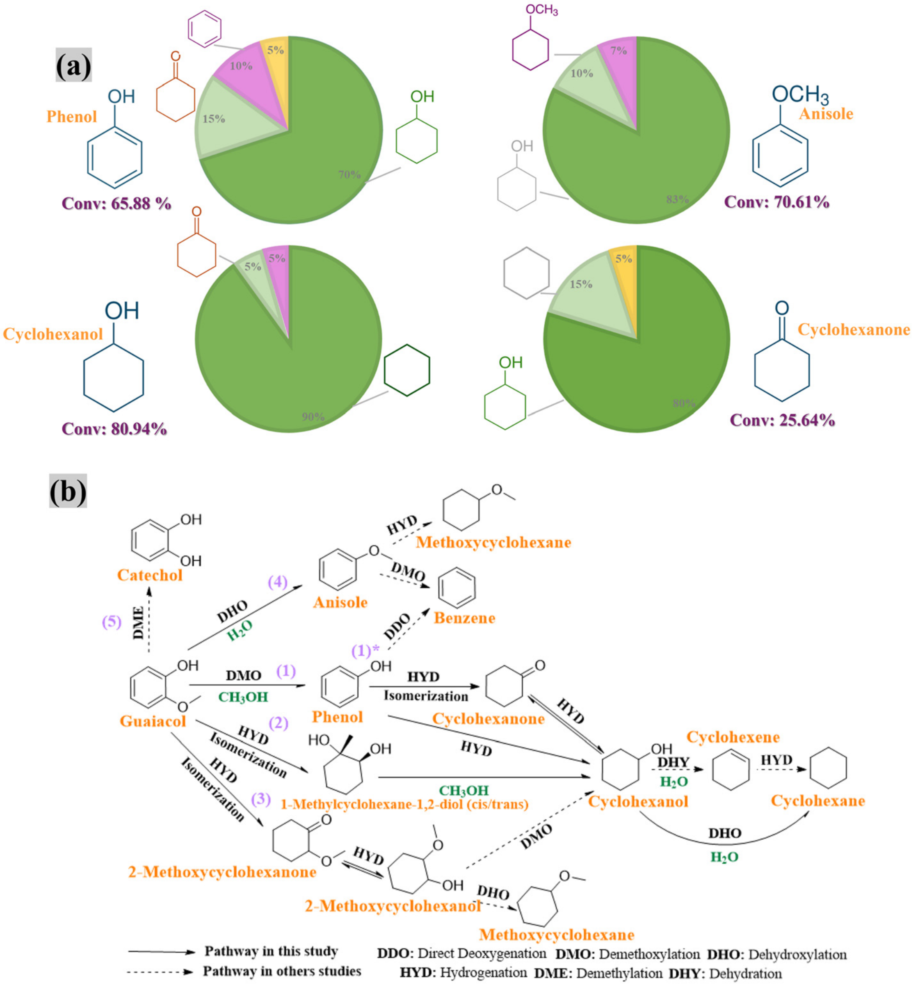

Fig. 8 (a) HDO of representative lignin-derived model compounds over the SiW_{12}-assisted $3Ni0.7Ru/TiO_2$ catalytic system (reaction conditions: 125 °C, 0.5 MPa H_2, 9 mL water, 0.12 g catalyst, 0.025 mol L^{-1} SiW_{12}, 0.5 mL substrate, and 1 h reaction time). (b) Proposed reaction pathway for guaiacol HDO to cyclohexanol over $3Ni0.7Ru/TiO_2$ in the SiW_{12}-assisted catalytic system.

cyclohexanol selectivity to 70.34%, accompanied by increased selectivity toward cyclohexane 13.47% and benzene 6.50%. These trends indicate that secondary reactions become more prominent at elevated temperatures, particularly the further deoxygenation of cyclohexanol to cyclohexane.[98] At this stage, two competing pathways are promoted: hydrogenolysis of the aromatic–O bond (Route 1*, Fig. 8b) and aromatic ring hydrogenation (Route 1, Fig. 8b). The aromatic–O bond exhibits a high bond dissociation energy (466 kJ mol^{-1}), making its cleavage more favorable at higher temperatures and thereby enhancing benzene formation.[4] In contrast, phenol hydrogenation is exothermic, and temperatures above 125 °C can thermodynamically suppress this step, limiting further phenol conversion.[99] Accordingly, 125 °C was identified as the optimal reaction temperature, providing a balance between conversion efficiency and favorable selectivity toward the desired HDO products.

The synergistic interaction between SiW_{12} and $3Ni0.7Ru/TiO_2$ enabled efficient guaiacol HDO under mild reaction conditions (0.5 MPa and 125 °C). This performance surpasses that of most previously reported catalysts (Fig. 7d and Table S3), which typically require longer reaction times (>6 h), higher H_2 pressures (>3 MPa), and elevated temperatures (>200 °C) to achieve comparable activity. These results suggest the exceptional performance of the SiW_{12}-assisted $3Ni0.7Ru/TiO_2$ catalytic system for the selective conversion of guaiacol to cyclohexanol.

3.4.3 Effect of catalyst loading and SiW_{12} concentration. Optimizing catalyst loading is crucial in HDO, as it governs the balance between active site availability and diffusion limitations, ultimately determining catalytic efficiency and product selectivity.[100] The influence of catalyst loading on guaiacol HDO was examined by adjusting the amount of $3Ni0.7Ru/TiO_2$ catalyst from 0.04 to 0.24 g (Fig. 7e). As the catalyst loading increased from 0.04 to 0.12 g, the guaiacol conversion rose markedly from 11.8% to 56.8%. This significant enhancement can be ascribed to the greater availability of active surface sites to react with SiW_{12}, which facilitates guaiacol adsorption, hydrogen dissociation, and an overall increase in reaction turnover frequency.[30,74] Furthermore, the additional surface sites facilitate more effective interaction with reduced $[SiW_{12}]^{5-}$ species, promoting hydrogen transfer to the catalyst surface.[21] Interestingly, the overall product distribution remained nearly constant across the different catalyst loadings, suggesting that the HDO primarily proceeds through the hydrogenation pathway (Route 1, Fig. 8d) and is largely governed by the availability of SiW_{12} as a hydrogen mediator.

To further elucidate the role of SiW_{12} in the reaction (Fig. 7f), its concentration was systematically varied from 0.008 and 0.05 mol L^{-1}. At 0.008 mol L^{-1}, the reaction favored cyclohexanol formation 47.19%, with only a minor yield of cyclohexane 6.42%. Increasing the concentration to 0.017 mol L^{-1} led to a modest enhancement in both products, with cyclohexanol and cyclohexane selectivity's rising to 49.42% and 11.00%, respectively. Notably, a further increase to 0.025 mol L^{-1} resulted in a substantial improvement in cyclohexanol selectivity 69.32%, accompanied by a pronounced decrease in cyclohexane selectivity to 2.65%. When the concentration was further increased to 0.05 mol L^{-1}, an overall decline in guaiacol conversion was observed. This behavior suggests that an optimum SiW_{12} concentration is required to balance hydrogen activation, hydrogen transfer, and substrate conversion. At higher SiW_{12} concentrations, excessive adsorption of SiW_{12} species on the catalyst surface may partially block active sites and hinder efficient interfacial hydrogen transfer, thereby reducing the overall reaction rate.[28] On this basis, 0.025 mol L^{-1} was identified as the optimal SiW_{12} concentration.

3.4.4 Effect of guaiacol-to-water phase ratio. The substrate loading is a key factor influencing both catalytic activity and product distribution in HDO reactions.[101] To examine this effect, the influence of guaiacol content on the reactivity of the $3Ni0.7Ru/TiO_2$ catalyst was investigated (Fig. S30). The results show that increasing the guaiacol amount beyond the optimum negatively affected conversion efficiency due to an imbalance between substrate concentration, hydrogen-transfer efficiency, and the availability of active catalytic sites within the system.[102] At the lowest guaiacol amount 0.25 mL, the conversion reached 40.55%, which may be associated with inefficient utilization of reactive hydrogen species mediated by the hydrogen-buffer system and competitive adsorption between hydrogen species, intermediates, and guaiacol molecules on the catalyst surface.[103] When the guaiacol amount increased to 0.50 mL, both guaiacol conversion 58.8% and cyclohexanol selectivity 73.73% increased significantly, indicating improved hydrogen-transfer efficiency and more effective utilization of the catalytic surface. However, further increasing the guaiacol amount to 1.0 mL resulted in a decline in conversion 56.84% together with increased phenol selectivity. Excess substrate additionally reduced cyclohexanol yield due to lower guaiacol conversion and the formation of by-products such as phenol and cyclohexanone. This decrease in activity is mainly attributed to surface site saturation and competitive adsorption among reactants and intermediates, which hinder hydrogen transfer and reduce overall reaction efficiency.[104] Additionally, the accumulation of oxygenated compounds on the catalyst surface may influence the availability of active metal sites, thereby reducing their ability to promote deoxygenation reactions effectively.[102]

To achieve complete conversion into the target product, the effect of reaction time on guaiacol conversion and product distribution was examined under optimized conditions (Fig. 7g). Extending the reaction time from 30 min to 3 h increased guaiacol conversion from 36.93% to 77.53%. During this period, the cyclohexanol selectivity decreased from 63.47% to 47.81%, while the selectivity of cyclohexanone 5.40% and phenol 0.85% were still detected. This indicates that guaiacol is converted to cyclohexanol through phenol and cyclohexanone as intermediate species (Route 1, Fig. 8b).[77] Further extending the reaction time beyond 3 h led to a continued decrease in cyclohexanol yield to 42.41% at 8 h, along with an increase in cyclohexane formation up to 31.58%. The nearly constant yield of cyclohexanone suggests that its conversion to cyclohexanol is a rate-limiting step, and that longer reaction times promote over-hydrogenation of cyclohexanol to cyclohexane.[99] Accordingly, a reaction time of 1 h was selected as optimal for maximizing cyclohexanol yield over the SiW_{12} with 3N0.7Ru/TiO_2 catalytic system.

3.4.5 Catalyst stability. Catalyst stability is a critical factor in evaluating its suitability for practical and industrial applications.[88] The detailed stability measurement procedure is provided in the SI, while the corresponding catalytic performance results are shown in (Fig. 7h), guaiacol conversion gradually decreased from about 60% in the first cycle to approximately 38–40% after the fifth cycle. Concurrently, the product distribution shifted noticeably. Cyclohexanol, the dominant product in the initial cycles with a selectivity of 60%, gradually declined to 25% by the fifth cycle, while cyclohexanone and 1-methyl-1,2-cyclohexanediol (*cis*, *trans*) became more pronounced. The observed deactivation is most likely associated with partial surface blockage caused by strongly adsorbed SiW_{12} species and/or the accumulation of reaction intermediates and water, which can hinder access to active metal sites and suppress H_2 dissociation.[88] XRD results, as shown in (Fig. S23) results further confirm the structural stability of the catalyst after exposure to the reaction environment. The characteristic diffraction peaks of 3Ni0.7Ru/TiO_2 remained largely unchanged after reaction, indicating that the catalyst structure remained intact. In addition, a broad feature observed in the 5–10° region was attributed to physically adsorbed SiW_{12} on the catalyst surface.[88] Consistent with the XRD results, Raman spectra in (Fig. S24a) retained the characteristic TiO_2 vibration modes before and after reaction, with only a slight decrease in intensity, likely due to surface coverage by physically adsorbed SiW_{12}. Furthermore, the O_2-TPO profiles in (Fig. S24b) revealed substantial suppression of carbonaceous deposition in the presence of dissolved SiW_{12}, indicating that the hydrogen-buffer-assisted system effectively inhibits the formation and accumulation of coke precursors during the HDO reaction. After regeneration (cycle 5*), the catalyst was completely separated from the reaction solution, thoroughly washed with ethanol, dried, and subsequently reduced again at 350 °C for 2 h under hydrogen. A fresh aqueous solution containing SiW_{12} was then introduced for the next reaction cycle. Both guaiacol conversion and cyclohexanol selectivity were partially restored after regeneration, reaching 47% conversion and 50% cyclohexanol selectivity. These results indicate that the catalyst deactivation was largely reversible and mainly associated with temporary surface coverage or adsorption effects rather than permanent structural degradation and can be reactivated through appropriate treatment. Overall, the catalyst exhibits acceptable recyclability and maintains reasonable activity under the studied conditions.

3.5 Proposed HDO pathway to cyclohexanol

The catalytic SiW_{12}-induced HDO of guaiacol over bimetallic NiRu-based catalysts is known to proceed *via* multiple, competitive pathways, as reported in prior studies.[36,77,80,99,105] Based on the distribution of intermediates and final products detected by GC-MS and FID-GC as shown in (Fig. S31 and S32), including phenol, anisole, cyclohexanol, 1-methyl-1,2-cyclohexanediol (*cis* and *trans*), with trace quantities of cyclohexane, benzene, methanol, methoxycyclohexanol, methoxycyclohexanone, 1,2-cyclohexanediol, and catechol we propose five mechanistic routes, as outlined in (Fig. 8b).

The reaction pathway of guaiacol over the SiW_{12} with suspended 3N0.7Ru/TiO_2 catalyst was elucidated by monitoring the temporal evolution of products and intermediates over an 8 hour reaction period. As shown in (Fig. 7g), phenol and cyclohexanone were identified in the early stages but gradually diminished over time, indicating their roles as transient intermediates. Concurrently, the yield of cyclohexanol increased steadily, reaching a maximum at 180 minutes before slightly declining as cyclohexane formation became more prominent. Minor increases in methoxycyclohexanol and methoxycyclohexanone were also observed, whereas anisole concentrations remained largely unchanged. The concentration of 1-methyl-1,2-cyclohexanediol initially increased but later plateaued, suggesting that this pathway is operative but not predominant. To validate the proposed reaction mechanism, control experiments were conducted using individual intermediates as substrates (Fig. 8a). When phenol was used, a conversion of 65.88% was achieved, yielding products such as cyclohexanone, cyclohexanol, benzene, and cyclohexane. These results confirm that Pathway I, involving initial demethoxylation of guaiacol to phenol followed by sequential hydrogenation, is the dominant reaction route under the tested conditions.[106] The negligible formation of catechol and consistent detection of methanol further support the prevalence of the demethoxylation pathway.[107] Anisole, the second substrate containing a methoxy ($-OCH_3$) substituent, exhibited a conversion of 70.61%, with selectivity of 80.5% toward cyclohexanol and 10.2% toward methoxycyclohexane. These results suggest that the methoxy group undergoes C–O bond cleavage through either demethylation or direct hydrogenolysis, followed by hydrogenation of the aromatic ring. Consequently, both cyclohexanol and methoxycyclohexane are formed as the main products.[108] Furthermore, the data suggest that while cyclohexanol can be further deoxygenated to cyclohexane at prolonged reaction times, this step is kinetically limited.[109] When cyclohexanol was used as the substrate, only 25.64% conversion to cyclohexane was observed. In contrast, when cyclohexanone was employed, 80.94% conversion to cyclohexanol was achieved, with 80% selectivity, highlighting the efficiency of the hydrogenation step relative to deoxygenation. We summarized the proposed pathway in (Fig. 8b). Pathway (1) involves the demethoxylation of guaiacol to phenol, followed by sequential hydrogenation to cyclohexanone and subsequently to cyclohexanol, which may undergo further hydrogenolysis to cyclohexane.[105] Pathway (2) proceeds *via* initial hydrogenation and isomerization to 1-methyl-1,2-cyclohexanediol (*cis*, *trans*), which is then dehydrated and demethylated to cyclohexanol.[109] Pathway (3) entails hydrogenation of the aromatic ring to yield 2-methoxycyclohexanone, which subsequently converted to methoxycyclohexane, were detected in very small amount, likely due to the catalyst's structural and electronic properties.[30] Pathway (4) describes dihydroxylation of guaiacol to anisole, followed by hydrogenation to methoxycyclohexane; however, anisole is typically observed as a stable intermediate due to the high bond dissociation energy (BDE) of the C(sp^2)–OH bond.[107] Pathway (5) involves demethylation to catechol *via* C(sp^3)–O bond cleavage, followed by hydrogenation to 1,2-cyclohexanediol. This route is generally less favored due to higher steric hindrance and activation barriers compared to demethoxylation.[107] In summary, our analysis suggests that the dominant reaction pathway in the SiW_{12}-assisted catalytic system is the demethoxylation of guaiacol to phenol, followed by aromatic ring hydrogenation to cyclohexanone and subsequently cyclohexanol, which is the major product under the optimized reaction conditions. In parallel, a minor pathway involves direct hydrogenation of the aromatic ring, accompanied by structural rearrangement to form 1-methyl-1,2-cyclohexanediol (*cis* and *trans*), which can subsequently be converted to cyclohexanol through dehydration and demethylation reactions, similar to previous study.[105] Upon prolonged reaction, cyclohexanol may undergo further deoxygenation through dehydration and hydrogenation steps, leading to the formation of cyclohexane, as observed in the extended reaction-time experiments (Fig. 7g).

4. Conclusions

In summary, a hydrogen-buffer-assisted catalytic system was developed by combining bimetallic Ni–M (M = Ru, Pt, Pd) catalysts with the reversible hydrogen buffer SiW_{12} for the HDO of lignin-derived phenolics under mild conditions. Among the catalysts investigated, the Ni–Ru/TiO_2 system exhibited the best catalytic performance, achieving high guaiacol conversion and cyclohexanol selectivity under mild temperature and hydrogen pressure. Mechanistic studies demonstrated that SiW_{12} plays a key role as a reversible hydrogen buffer, facilitating hydrogen transfer through its proton–electron redox cycle, facilitating hydrogen transfer in the liquid phase and improving hydrogen utilization during the reaction. This process improves hydrogen availability in the aqueous phase and enhances the efficiency of hydrogen utilization during the reaction. Simultaneously, *in situ* interaction of SiW_{12} with the catalyst surface generates a metal–acid interface that promotes hydrogen spillover, interfacial hydrogen exchange, and efficient C–O bond activation. The synergistic interaction between the Ni–Ru active sites and the SiW_{12} hydrogen buffer promotes efficient C–O bond cleavage and selective hydrogenation of aromatic intermediates, enabling the selective formation of cyclohexanol while suppressing carbonaceous deposition under multiphase conditions. The catalyst also exhibited good stability and recyclability during repeated reaction cycles. Overall, this work introduces a hydrogen-pathway engineering strategy for bimetallic catalysts that extends beyond conventional hydrogen activation by integrating heterogeneous hydrogen activation with homogeneous proton–electron hydrogen transfer. This approach provides new insights into hydrogen management in aqueous-phase catalysis and offers a promising direction for designing efficient catalytic systems for sustainable biomass upgrading under mild conditions.

Author contributions

Reem Shomal: conceptualization, methodology, investigation, validation, formal analysis, data curation, and writing – original draft. Ying Zheng: conceptualization, methodology, resources, supervision, validation, funding acquisition, and writing – review & editing.

Conflicts of interest

The authors declare that they have no known financial or personal relationships that could have influenced or appeared to influence the work reported in this paper.

Data availability

All data supporting the findings of this study are included in the manuscript and the Supplementary Information (SI), which is available at https://doi.org/10.1039/d6gc02407f. The Supplementary Information provides detailed experimental methods, catalyst preparation and characterization, additional catalytic performance results, and supporting figures and tables. Any additional data related to this study are available from the corresponding author upon reasonable request.

Acknowledgements

The authors would like to express their gratitude for the financial support provided by the Natural Science and Engineering Research Council of Canada (NSERC) and the Canada Chair Program.

References

1 R. Shomal and Y. Zheng, Development of Processes and Catalysts for Biomass to Hydrocarbons at Moderate Conditions: A Comprehensive Review, *Nanomaterials*, 2023, **13**, 2845, DOI: 10.3390/nano13212845.

2 Z. Zhang, X. Wang, C. Wang, Z. Yan, G. Zhuang, N. Ma and Q. Li, Selective hydrodeoxygenation of bio-oil model compounds and mixtures over CuCoOx catalysts under mild conditions, *Chem. Eng. J.*, 2024, **483**, 149367, DOI: 10.1016/j.cej.2024.149367.

3 V. N. Bui, D. Laurenti, P. Afanasiev and C. Geantet, Hydrodeoxygenation of guaiacol with CoMo catalysts. Part I: Promoting effect of cobalt on HDO selectivity and

activity, *Appl. Catal., B*, 2011, **101**, 239–245, DOI: 10.1016/j.apcatb.2010.10.025.

4 T. M. Huynh, U. Armbruster, C. R. Kreyenschulte, L. H. Nguyen, B. M. Q. Phan, D. A. Nguyen and A. Martin, Understanding the Performance and Stability of Supported Ni-Co-Based Catalysts in Phenol HDO, *Catalysts*, 2016, **6**, 176, DOI: 10.3390/catal6110176.

5 C. Chen, W. Chen, M. Zhou, Y. Xiong, X. Ji, M. Zhou, L. Zhang, X. Rao and J. Jiang, Co-ZIF reinforced kraft lignin biochar as an efficient catalyst for highly selective hydrodeoxygenation of lignin-derived chemicals, *Chem. Eng. J.*, 2024, **492**, 152353, DOI: 10.1016/j.cej.2024.152353.

6 Z. Jiang, W. Wan, Z. Lin, J. Xie and J. G. Chen, Understanding the Role of M/Pt(111) (M = Fe, Co, Ni, Cu) Bimetallic Surfaces for Selective Hydrodeoxygenation of Furfural, *ACS Catal.*, 2017, **7**, 5758–5765, DOI: 10.1021/acscatal.7b01682.

7 C. Li, Y. Nakagawa, M. Yabushita, A. Nakayama and K. Tomishige, Guaiacol Hydrodeoxygenation over Iron–Ceria Catalysts with Platinum Single-Atom Alloy Clusters as a Promoter, *ACS Catal.*, 2021, **11**, 12794–12814, DOI: 10.1021/acscatal.1c03539.

8 Q. Lai, C. Zhang and J. H. Holles, Hydrodeoxygenation of guaiacol over Ni@Pd and Ni@Pt bimetallic overlayer catalysts, *Appl. Catal., A*, 2016, **528**, 1–13, DOI: 10.1016/j.apcata.2016.09.009.

9 S. Hidayat, J. Han, J. Kim, H. T. Hwang, X. Zhou, J. I. Choi, H. Zhang, D.-Y. Hong, J.-M. Ha and S.-S. Kim, Selective hydrodeoxygenation of BHET using bimetallic Pt–Sn/γ-Al_2O_3 catalysts: Catalyst design, reaction pathway, and performance evaluation, *Fuel Process. Technol.*, 2025, **280**, 108367, DOI: 10.1016/j.fuproc.2025.108367.

10 Y. Shu, L. E. Murillo, J. P. Bosco, W. Huang, A. I. Frenkel and J. G. Chen, The effect of impregnation sequence on the hydrogenation activity and selectivity of supported Pt/Ni bimetallic catalysts, *Appl. Catal., A*, 2008, **339**, 169–179, DOI: 10.1016/j.apcata.2008.01.024.

11 A. Álvarez M, M. Á. Centeno and J. A. Odriozola, Ru–Ni Catalyst in the Combined Dry-Steam Reforming of Methane: The Importance in the Metal Order Addition, *Top. Catal.*, 2016, **59**, 303–313, DOI: 10.1007/s11244-015-0426-5.

12 B. Li, S. Kado, Y. Mukainakano, T. Miyazawa, T. Miyao, S. Naito, K. Okumura, K. Kunimori and K. Tomishige, Surface modification of Ni catalysts with trace Pt for oxidative steam reforming of methane, *J. Catal.*, 2007, **245**, 144–155, DOI: 10.1016/j.jcat.2006.10.004.

13 X. Wang, M. Arai, Q. Wu, C. Zhang and F. Zhao, Hydrodeoxygenation of lignin-derived phenolics – a review on the active sites of supported metal catalysts, *Green Chem.*, 2020, **22**, 8140–8168, DOI: 10.1039/D0GC02610G.

14 X. Yu and C. T. Williams, Recent applications of nickel and nickel-based bimetallic catalysts for hydrodeoxygenation of biomass-derived oxygenates to fuels, *Catal. Sci. Technol.*, 2023, **13**, 802–825, DOI: 10.1039/D2CY01179D.

15 J. Lee, Y. T. Kim and G. W. Huber, Aqueous-phase hydrogenation and hydrodeoxygenation of biomass-derived oxygenates with bimetallic catalysts, *Green Chem.*, 2014, **16**, 708–718, DOI: 10.1039/C3GC41071D.

16 S. Oh, J. H. Lee, I.-G. Choi and J. W. Choi, Enhancement of bio-oil hydrodeoxygenation activity over Ni-based bimetallic catalysts supported on SBA-15, *Renewable Energy*, 2020, **149**, 1–10, DOI: 10.1016/j.renene.2019.12.027.

17 A. M. Robinson, J. E. Hensley and J. W. Medlin, Bifunctional Catalysts for Upgrading of Biomass-Derived Oxygenates: A Review, *ACS Catal.*, 2016, **6**, 5026–5043, DOI: 10.1021/acscatal.6b00923.

18 S. T. Ceyer, The Unique Chemistry of Hydrogen beneath the Surface: Catalytic Hydrogenation of Hydrocarbons, *Acc. Chem. Res.*, 2001, **34**, 737–744, DOI: 10.1021/ar970030f.

19 J. Zhang and C. Zhao, Development of a Bimetallic Pd-Ni/HZSM-5 Catalyst for the Tandem Limonene Dehydrogenation and Fatty Acid Deoxygenation to Alkanes and Arenes for Use as Biojet Fuel, *ACS Catal.*, 2016, **6**, 4512–4525, DOI: 10.1021/acscatal.6b00520.

20 K. A. Rogers and Y. Zheng, Selective Deoxygenation of Biomass-Derived Bio-oils within Hydrogen-Modest Environments: A Review and New Insights, *ChemSusChem*, 2016, **9**, 1750–1772, DOI: 10.1002/cssc.201600144.

21 W. Liu, W. You, W. Sun, W. Yang, A. Korde, Y. Gong and Y. Deng, Ambient-pressure and low-temperature upgrading of lignin bio-oil to hydrocarbons using a hydrogen buffer catalytic system, *Nat. Energy*, 2020, **5**, 759–767, DOI: 10.1038/s41560-020-00680-x.

22 A. Robinson, G. A. Ferguson, J. R. Gallagher, S. Cheah, G. T. Beckham, J. A. Schaidle, J. E. Hensley and J. W. Medlin, Enhanced Hydrodeoxygenation of m-Cresol over Bimetallic Pt–Mo Catalysts through an Oxophilic Metal-Induced Tautomerization Pathway, *ACS Catal.*, 2016, **6**, 4356–4368, DOI: 10.1021/acscatal.6b01131.

23 H. Shi, Valorization of Biomass-derived Small Oxygenates: Kinetics, Mechanisms and Site Requirements of H2-involved Hydrogenation and Deoxygenation Pathways over Heterogeneous Catalysts, *ChemCatChem*, 2019, **11**, 1824–1877, DOI: 10.1002/cctc.201801828.

24 R. Tyburski, T. Liu, S. D. Glover and L. Hammarström, Proton-Coupled Electron Transfer Guidelines, Fair and Square, *J. Am. Chem. Soc.*, 2021, **143**, 560–576, DOI: 10.1021/jacs.0c09106.

25 M. H. V. Huynh and T. J. Meyer, Proton-Coupled Electron Transfer, *Chem. Rev.*, 2007, **107**, 5004–5064, DOI: 10.1021/cr0500030.

26 X. Gao, R. Ma, Z. Liu, S. Wang, Y. Wu and G. Song, Hydrodeoxygenation of lignin-derived phenols into cycloalkanes by atomically dispersed Pt-polyoxometalate catalysts, *Appl. Catal., B*, 2024, **352**, 124059, DOI: 10.1016/j.apcatb.2024.124059.

27 R. Shu, H. Jiang, L. Xie, X. Liu, T. Yin, Z. Tian, C. Wang and Y. Chen, Efficient hydrodeoxygenation of lignin-derived phenolic compounds by using Ru-based biochar

catalyst coupled with silicotungstic acid, *Renewable Energy*, 2023, **202**, 1160–1168, DOI: 10.1016/j.renene.2022.11.092.

28 L. Wang, F. Yan, W. Sun, B. Dai, W. Liu, S.-L. Chen and Y. Deng, Ambient-pressure and low-temperature hydrogenation of nitrogen to ammonia in a synergetic catalytic system, *Chem. Eng. J.*, 2024, **493**, 152506, DOI: 10.1016/j.cej.2024.152506.

29 R. Zhang, W. Sun, Y. Zhang, Y. Feng, B. Dai and Y. Deng, Photocatalytic hydrogen production from alcohols to *in situ* hydrogenation of nitrogen to ammonia by a dual-catalyst system, *Appl. Catal., B*, 2024, **358**, 124429, DOI: 10.1016/j.apcatb.2024.124429.

30 R. Shomal and Y. Zheng, Bifunctional hydrogen buffer catalytic system forenhanced hydrodeoxygenation of guaiacol under mild conditions, *Chem. Eng. J.*, 2025, **516**, 164021, DOI: 10.1016/j.cej.2025.164021.

31 K. Alharbi, E. F. Kozhevnikova and I. V. Kozhevnikov, Hydrogenation of ketones over bifunctional Pt-heteropoly acid catalyst in the gas phase, *Appl. Catal., A*, 2015, **504**, 457–462, DOI: 10.1016/j.apcata.2014.10.032.

32 K. Alharbi, W. Alharbi, E. F. Kozhevnikova and I. V. Kozhevnikov, Deoxygenation of Ethers and Esters over Bifunctional Pt–Heteropoly Acid Catalyst in the Gas Phase, *ACS Catal.*, 2016, **6**, 2067–2075, DOI: 10.1021/acscatal.6b00096.

33 H. Althikrallah, E. F. Kozhevnikova and I. V. Kozhevnikov, Hydrodeoxygenation of 2,5-dimethyltetrahydrofuran over bifunctional metal-acid catalyst Pt–Cs2.5H0.5PW12O40 in the gas phase: Kinetics and mechanism, *Mol. Catal.*, 2021, **510**, 111711, DOI: 10.1016/j.mcat.2021.111711.

34 O. Poole, K. Alharbi, D. Belic, E. F. Kozhevnikova and I. V. Kozhevnikov, Hydrodeoxygenation of 3-pentanone over bifunctional Pt-heteropoly acid catalyst in the gas phase: Enhancing effect of gold, *Appl. Catal., B*, 2017, **202**, 446–453, DOI: 10.1016/j.apcatb.2016.09.044.

35 S. Itagaki, N. Matsuhashi, K. Taniguchi, K. Yamaguchi and N. Mizuno, Efficient Hydrodeoxygenation of Ketones, Phenols, and Ethers Promoted by Platinum–Heteropolyacid Bifunctional Catalysts, *Chem. Lett.*, 2014, **43**, 1086–1088, DOI: 10.1246/cl.140342.

36 O. U. Valdés-Martínez, V. A. Suárez-Toriello, J. A. de los Reyes, B. Pawelec and J. L. G. Fierro, Support effect and metals interactions for NiRu/Al$_2$O$_3$, TiO2 and ZrO2 catalysts in the hydrodeoxygenation of phenol, *Catal. Today*, 2017, **296**, 219–227, DOI: 10.1016/j.cattod.2017.04.007.

37 E. T. Kho, J. Scott and R. Amal, Ni/TiO2 for low temperature steam reforming of methane, *Chem. Eng. Sci.*, 2016, **140**, 161–170, DOI: 10.1016/j.ces.2015.10.021.

38 S. Tada, R. Kikuchi, A. Takagaki, T. Sugawara, S. T. Oyama, K. Urasaki and S. Satokawa, Study of RuNi/TiO2 catalysts for selective CO methanation, *Appl. Catal., B*, 2013, **140–141**, 258–264, DOI: 10.1016/j.apcatb.2013.04.024.

39 J. Chen, C. Chen, M. Qin, B. Li, B. Lin, Q. Mao, H. Yang, B. Liu and Y. Wang, Reversible hydrogen spillover in Ru-WO3-x enhances hydrogen evolution activity in neutral pH water splitting, *Nat. Commun.*, 2022, **13**, 5382, DOI: 10.1038/s41467-022-33007-3.

40 Y. Sun, Y. Bao, D. Yin, X. Bu, Y. Zhang, K. Yue, X. Qi, Z. Cai, Y. Li, X. Hu, J. C. Ho and X. Wang, Oxygen vacancy-induced efficient hydrogen spillover in Ni17W3/WO3−x/MoO3−x for a superior pH-universal hydrogen evolution reaction, *J. Mater. Chem. A*, 2024, **12**, 11563–11570, DOI: 10.1039/D4TA00729H.

41 A. Sreenavya, P. Aswin, V. Ganesh, N. J. Venkatesha and A. Sakthivel, Facile water-free synthesis of noble metal-containing hydrotalcites-derived materials and their application for hydrotreatment of anisole, *Mater. Today Sustainability*, 2022, **18**, 100153, DOI: 10.1016/j.mtsust.2022.100153.

42 Z. Guo, Q. Huang, S. Luo and W. Chu, Atmospheric Discharge Plasma Enhanced Preparation of Pd/TiO2 Catalysts for Acetylene Selective Hydrogenation, *Top. Catal.*, 2017, **60**, 1009–1015, DOI: 10.1007/s11244-017-0766-4.

43 V. G. Deshmane, S. L. Owen, R. Y. Abrokwah and D. Kuila, Mesoporous nanocrystalline TiO2 supported metal (Cu, Co, Ni, Pd, Zn, and Sn) catalysts: Effect of metal-support interactions on steam reforming of methanol, *J. Mol. Catal. A: Chem.*, 2015, **408**, 202–213, DOI: 10.1016/j.molcata.2015.07.023.

44 I. Faturachman, H. H. Kurniawan, R. T. Yunarti, R. R. Widjaya, A. A. Dwiatmoko, Y. Maryati and N. Rinaldi, Pd–Ni bimetallic nanoparticles supported on TiO2 as an efficient catalyst for catalytic transfer hydrodeoxygenation of guaiacol, *Can. J. Chem.*, 2022, **100**, 583–588, DOI: 10.1139/cjc-2021-0330.

45 T. Wei, X. Zhao, L. Li, L. Wang, S. Lv, L. Gao, G. Yuan and L. Li, Enhanced Formaldehyde Oxidation Performance of the Mesoporous TiO2(B)-Supported Pt Catalyst: The Role of Hydroxyls, *ACS Omega*, 2022, **7**, 25491–25501, DOI: 10.1021/acsomega.2c02490.

46 S. Zou, L. Cao, X. Zhang, C. Chen, M. Tada, S. Muratsugu, R. Tian, H. Sun, A. Li, X. Han, X. Liao, J. Huang and A. R. Masri, 'Tearing Effect' of Alloy–Support Interaction for Alloy Redispersion in NiRu/TiO2 Hydrogenation Catalysts, *Angew. Chem., Int. Ed.*, 2025, **64**, e202425066, DOI: 10.1002/anie.202425066.

47 Y. Guo, Z. Chen, R. M. Rioux and P. E. Savage, Hydrothermal reaction of tryptophan over Ni-based bimetallic catalysts, *J. Supercrit. Fluids*, 2019, **143**, 336–345, DOI: 10.1016/j.supflu.2018.09.006.

48 X. Xu, F. Liu, J. Huang, W. Luo, J. Yu, X. Fang, O. E. Lebedeva and X. Wang, The Influence of RuO2 Distribution and Dispersion on the Reactivity of RuO2–SnO2 Composite Oxide Catalysts Probed by CO Oxidation, *ChemCatChem*, 2019, **11**, 2473–2483, DOI: 10.1002/cctc.201802095.

49 B. Cui, H. Wang, Q. Ge and X. Zhu, Size-Dependent Strong Metal–Support Interactions of Rutile TiO2-Supported Ni Catalysts for Hydrodeoxygenation of

m-Cresol, *Catalysts*, 2022, **12**, 955, DOI: 10.3390/catal12090955.

50 D. Messou, V. Bernardin, F. Meunier, M. B. Ordoño, A. Urakawa, B. F. Machado, V. Collière, R. Philippe, P. Serp and C. L. Berre, Origin of the synergistic effect between TiO2 crystalline phases in the Ni/TiO2-catalyzed CO2 methanation reaction, *J. Catal.*, 2021, **398**, 14–28, DOI: 10.1016/j.jcat.2021.04.004.

51 Y. Geng and H. Li, Hydrogen Spillover-Enhanced Heterogeneously Catalyzed Hydrodeoxygenation for Biomass Upgrading, *ChemSusChem*, 2022, **15**, e202102495, DOI: 10.1002/cssc.202102495.

52 H. Yu, X. Yang, Y. Wu, Y. Guo, S. Li, W. Lin, X. Li and J. Zheng, Bimetallic Ru-Ni/TiO2 catalysts for hydrogenation of N-ethylcarbazole: Role of TiO2 crystal structure, *J. Energy Chem.*, 2020, **40**, 188–195, DOI: 10.1016/j.jechem.2019.04.009.

53 X. Ning, Y. Sun, H. Fu, X. Qu, Z. Xu and S. Zheng, N-doped porous carbon supported Ni catalysts derived from modified Ni-MOF-74 for highly effective and selective catalytic hydrodechlorination of 1,2-dichloroethane to ethylene, *Chemosphere*, 2020, **241**, 124978, DOI: 10.1016/j.chemosphere.2019.124978.

54 R. Shu, Y. Chen, Y. Lin, Y. Deng, Y. Liu, K. Li, T. Yin, Z. Ma and J. Long, Synergistic effects of Ni-Ni3P and Lewis-Brønsted acid for enhanced hydrodeoxygenation of phenolic compounds over Ni-Ni3P/ZrP, *Appl. Catal., B*, 2026, **383**, 126096, DOI: 10.1016/j.apcatb.2025.126096.

55 X. Jiang, M. Manawan, T. Feng, R. Qian, T. Zhao, G. Zhou, F. Kong, Q. Wang, S. Dai and J. H. Pan, Anatase and rutile in evonik aeroxide P25: Heterojunctioned or individual nanoparticles?, *Catal. Today*, 2018, **300**, 12–17, DOI: 10.1016/j.cattod.2017.06.010.

56 F. Liang, J. Zhang, L. Zheng, C.-K. Tsang, H. Li, S. Shu, H. Cheng and Y. Y. Li, Selective electrodeposition of Ni into the intertubular voids of anodic TiO2 nanotubes for improved photocatalytic properties, *J. Mater. Res.*, 2013, **28**, 405–410, DOI: 10.1557/jmr.2012.380.

57 M. Li, H. Wang, W. Zhu, W. Li, C. Wang and X. Lu, RuNi Nanoparticles Embedded in N-Doped Carbon Nanofibers as a Robust Bifunctional Catalyst for Efficient Overall Water Splitting, *Adv. Sci.*, 2020, **7**, 1901833, DOI: 10.1002/advs.201901833.

58 X. Sun, J. Liu, Y. Du, M. Shen, K. Liu, Z. Liang, W. Cheng, J. Chen and X. F. Lu, Bifunctional Arrays of NiRu Single-Atom Alloy Nanoparticles Confined in a Porous Carbon Nanosheet for Sustained Anion-Exchange Membrane Water Electrolysis, *Nano Lett.*, 2025, **25**, 11680–11688, DOI: 10.1021/acs.nanolett.5c02754.

59 L. Yang, Z. Ni, Y. Zhao, Y. Long, M. Xi, A. Chen and H. Zhang, Interfacial Electric Field Stabilized Ru Single-Atom Catalysts for Efficient Water Oxidation, *ACS Catal.*, 2024, **14**(14), DOI: 10.1021/acscatal.4c01829.

60 Q. He, Y. Zhou, L. Mou, C. Wu, D. Liu, B. Ge, J. Jiang and L. Song, Iron-doped ruthenium with a good interfacial environment achieving superior hydrogen evolution activity under alkaline conditions, *Energy Environ. Sci.*, 2025, **18**, 1984–1991, DOI: 10.1039/D4EE05356G.

61 X. Xie, Y. Zhang, Y. Qin, J. Wu, M. Lei, K. Huang, R. Wang and P. Du, Bifunctional mixed-valence ruthenium heterostructure for robust electrocatalytic water splitting in acid media, *Adv. Compos. Hybrid Mater.*, 2025, **8**, 133, DOI: 10.1007/s42114-025-01234-z.

62 X. Chen, X.-T. Wang, J.-B. Le, S.-M. Li, X. Wang, Y.-J. Zhang, P. Radjenovic, Y. Zhao, Y.-H. Wang, X.-M. Lin, J.-C. Dong and J.-F. Li, Revealing the role of interfacial water and key intermediates at ruthenium surfaces in the alkaline hydrogen evolution reaction, *Nat. Commun.*, 2023, **14**, 5289, DOI: 10.1038/s41467-023-41030-1.

63 K. Wachi, M. Makizawa, T. Aihara, S. Kiyohara, Y. Kumagai and K. Kamata, Oxygen Defect Engineering of Hexagonal Perovskite Oxides to Boost Catalytic Performance for Aerobic Oxidation of Sulfides to Sulfones, *Adv. Funct. Mater.*, 2025, **35**, 2425452, DOI: 10.1002/adfm.202425452.

64 F. Yang, L. Zhang, F. Li, Z. Zhang, L. Cui, R. Li, C. Fan and J. Liu, Enhanced photocatalytic hydrogen evolution of Ru/TiO2-x via oxygen vacancy-assisted hydrogen spillover process, *J. Colloid Interface Sci.*, 2023, **650**, 294–303, DOI: 10.1016/j.jcis.2023.06.206.

65 S. Wang, Y. Liu, M. Zhang, F. Li, Y. Chen and H. Song, Construction of a highly active and water-resistant Ni-based catalyst for the HDO reaction of phenol, *Sustainable Energy Fuels*, 2022, **6**, 4183–4196, DOI: 10.1039/D2SE00918H.

66 Z. Zou, Y. Shen, X. Zhang, W. Li, C. Chen, D. Fan, H. Zhang, H. Zhao and G. Wang, Toward High-Performance Hydrogenation at Room Temperature Through Tailoring Nickel Catalysts Stable in Aqueous Solution, *Adv. Sci.*, 2024, **11**, 2309303, DOI: 10.1002/advs.202309303.

67 T. Agladze, Y. Kolotyrkin and L. Janibakhchieva, The passivation of newly generated surface and kinetics of anodic dissolution of nickel, *Corros. Sci.*, 1990, **31**, 607–614, DOI: 10.1016/0010-938X(90)90169-6.

68 D. P. Satpute, G. N. Vaidya, S. K. Lokhande, S. D. Shinde, S. M. Bhujbal, D. R. Chatterjee, P. Rana, A. Venkatesh, M. Nagpure and D. Kumar, Organic reactions in aqueous media catalyzed by nickel, *Green Chem.*, 2021, **23**, 6273–6300, DOI: 10.1039/D1GC01983J.

69 Y. Cui and W. Liu, Synergistic effect between noble metal M (M = Pt, Pd, Rh) and polyoxometalate solution (H3PMo12O40) to catalyze and oxidize butanol under thermal condition and their application in the fuel cell, *J. Mater. Sci.:Mater. Electron.*, 2020, **31**, 15954–15959, DOI: 10.1007/s10854-020-04156-2.

70 G. Lee, S. E. Jun, J. Lim, J. Kim, H. Lee, W. S. Cheon, G. W. Ryoo, B.-G. Cho, S. Lee, M. S. Kwon, I.-H. Park, H. W. Jang, S. H. Park and K. C. Kwon, Tuning Hydrogen Binding on Ru Sites by Ni Alloying on MoO2 Enables Efficient Alkaline Hydrogen Evolution for Anion Exchange Membrane Water Electrolysis, *Adv. Sci.*, 2025, **12**, 2414622, DOI: 10.1002/advs.202414622.

71 J. Zhao, R. Urrego-Ortiz, N. Liao, F. Calle-Vallejo and J. Luo, Rationally designed Ru catalysts supported on TiN for highly efficient and stable hydrogen evolution in alkaline conditions, *Nat. Commun.*, 2024, **15**, 6391, DOI: 10.1038/s41467-024-50691-5.

72 J. Zhou, Z. Gao, G. Xiang, T. Zhai, Z. Liu, W. Zhao, X. Liang and L. Wang, Interfacial compatibility critically controls Ru/TiO2 metal-support interaction modes in CO2 hydrogenation, *Nat. Commun.*, 2022, **13**, 327, DOI: 10.1038/s41467-021-27910-4.

73 M. Allés, L. Meng, I. Beltrán, F. Fernández and F. Viñes, Atomic Hydrogen Interaction with Transition Metal Surfaces: A High-Throughput Computational Study, *J. Phys. Chem. C*, 2024, **128**, 20129–20139, DOI: 10.1021/acs.jpcc.4c06194.

74 M. Saleheen, O. Mamun, A. Mohan Verma, D. Sahsah and A. Heyden, Understanding the influence of solvents on the Pt-catalyzed hydrodeoxygenation of guaiacol, *J. Catal.*, 2023, **425**, 212–232, DOI: 10.1016/j.jcat.2023.06.009.

75 P. Kashyap, M. Jędrzejczyk, M. Gu, S. N. Steinmann, D. Kubička, N. Keller, C. Michel and A. M. Ruppert, Ru/TiO2 catalysts for selective formation of ring hydrogenation or ring-opening products from biomass-derived 5-hydroxymethylfurfural, *Green Chem.*, 2026, **28**, 7768–7781, DOI: 10.1039/D5GC06439B.

76 T. Li, H. Li, G. Huang, X. Shen, S. Wang and C. Li, Transforming biomass tar into a highly active Ni-based carbon-supported catalyst for selective hydrogenation-transalkylation of guaiacol, *J. Anal. Appl. Pyrolysis*, 2021, **153**, 104976, DOI: 10.1016/j.jaap.2020.104976.

77 B. Güvenatam, O. Kurşun, E. H. J. Heeres, E. A. Pidko and E. J. M. Hensen, Hydrodeoxygenation of mono- and dimeric lignin model compounds on noble metal catalysts, *Catal. Today*, 2014, **233**, 83–91, DOI: 10.1016/j.cattod.2013.12.011.

78 K. D. Jordan, J. A. Michejda and P. D. Burrow, Electron transmission studies of the negative ion states of substituted benzenes in the gas phase, *J. Am. Chem. Soc.*, 1976, **98**, 7189–7191, DOI: 10.1021/ja00439a014.

79 H. Ohta, H. Kobayashi, K. Hara and A. Fukuoka, Hydrodeoxygenation of phenols as lignin models under acid-free conditions with carbon-supported platinum catalysts, *Chem. Commun.*, 2011, **47**, 12209–12211, DOI: 10.1039/C1CC14859A.

80 A. Gutierrez, R. K. Kaila, M. L. Honkela, R. Slioor and A. O. I. Krause, Hydrodeoxygenation of guaiacol on noble metal catalysts, *Catal. Today*, 2009, **147**, 239–246, DOI: 10.1016/j.cattod.2008.10.037.

81 C. Zhao, Y. Kou, A. A. Lemonidou, X. Li and J. A. Lercher, Highly Selective Catalytic Conversion of Phenolic Bio-Oil to Alkanes, *Angew. Chem.*, 2009, **121**, 4047–4050, DOI: 10.1002/ange.200900404.

82 J. Wildschut, I. Melián-Cabrera and H. J. Heeres, Catalyst studies on the hydrotreatment of fast pyrolysis oil, *Appl. Catal., B*, 2010, **99**, 298–306, DOI: 10.1016/j.apcatb.2010.06.036.

83 J. Shangguan, N. Pfriem and Y.-H. (Cathy) Chin, Mechanistic details of CO bond activation in and H-addition to guaiacol at water-Ru cluster interfaces, *J. Catal.*, 2019, **370**, 186–199, DOI: 10.1016/j.jcat.2018.11.036.

84 C. Nania, M. Bertini, L. Gueci, F. Ferrante and D. Duca, DFT insights into competing mechanisms of guaiacol hydrodeoxygenation on a platinum cluster, *Phys. Chem. Chem. Phys.*, 2023, **25**, 10460–10471, DOI: 10.1039/D2CP06077A.

85 J. Lu and A. Heyden, Theoretical investigation of the reaction mechanism of the hydrodeoxygenation of guaiacol over a Ru(0 0 0 1) model surface, *J. Catal.*, 2015, **321**, 39–50, DOI: 10.1016/j.jcat.2014.11.003.

86 C. Chiu, A. Genest, A. Borgna and N. Rösch, Hydrodeoxygenation of Guaiacol over Ru(0001): A DFT Study, *ACS Catal.*, 2014, **4**, 4178–4188, DOI: 10.1021/cs500911j.

87 G. Liu, J. Zhang, H. Ren, Y. Tang and H. Sun, Optimizing the hydrogen adsorption strength on interfacial Ru sites with WN for high-efficiency hydrogen evolution, *Mater. Chem. Front.*, 2023, **7**, 4100–4108, DOI: 10.1039/D3QM00483J.

88 S. Li, L. Yan, Q. Liu, J. Liu, Q. Liu, W. Fan, X. Zhao, X. Zhang, C. Wang, L. Ma and Q. Zhang, One-pot hydrodeoxygenation of biomass furan derivatives into decane under mild conditions over Pd/C combined with phosphotungstic acid, *Green Chem.*, 2020, **22**, 2889–2900, DOI: 10.1039/D0GC00428F.

89 J. T. Miller, B. L. Meyers, F. S. Modica, G. S. Lane, M. Vaarkamp and D. C. Koningsberger, Hydrogen Temperature-Programmed Desorption (H2 TPD) of Supported Platinum Catalysts, *J. Catal.*, 1993, **143**, 395–408, DOI: 10.1006/jcat.1993.1285.

90 H. Jin, X. Yi, X. Sun, B. Qiu, W. Fang, W. Weng and H. Wan, Influence of H4SiW12O40 loading on hydrocracking activity of non-sulfide Ni–H4SiW12O40/SiO_2 catalysts, *Fuel*, 2010, **89**, 1953–1960, DOI: 10.1016/j.fuel.2009.11.031.

91 P. Marimuthu, T. Raja and R. Vinu, Hydrodeoxygenation of Guaiacol to Cyclohexanol Using Noble Metal-Supported Ni-Based Perovskite-Derived Catalysts, *ChemCatChem*, 2025, **17**, e00577, DOI: 10.1002/cctc.202500577.

92 B. Qiu, X. Yi, L. Lin, W. Fang and H. Wan, The hydrocracking of *n*-decane over bifunctional Ni-H3PW12O40/SiO_2 catalysts, *Catal. Today*, 2008, **131**, 464–471, DOI: 10.1016/j.cattod.2007.10.095.

93 Y. Zhang, W. Sun, R. Zhang, Y. Feng, B. Dai and J. Liu, Electrochemical hydrogenation of nitrogen to ammonia under ambient conditions in a suspended dual-catalyst system, *Green Chem.*, 2025, **27**, 2404–2416, DOI: 10.1039/D4GC05276E.

94 B. Wang, H. Zhao, Y. Cai, Y. Yang, Y. Lv and P. Liu, Highly Efficient Selective Hydrodeoxygenation of Guaiacol to Cyclohexanol over Co/ZrSi-x Catalysts, *Ind. Eng. Chem. Res.*, 2025, **64**, 1104–1116, DOI: 10.1021/acs.iecr.4c03832.

95 N. Joshi and A. Lawal, Hydrodeoxygenation of acetic acid in a microreactor, *Chem. Eng. Sci.*, 2012, **84**, 761–771, DOI: 10.1016/j.ces.2012.09.018.

96 L. Jiang, H. Guo, C. Li, P. Zhou and Z. Zhang, Selective cleavage of lignin and lignin model compounds without external hydrogen, catalyzed by heterogeneous nickel catalysts, *Chem. Sci.*, 2019, **10**, 4458–4468, DOI: 10.1039/C9SC00691E.

97 R. Dang, X. Ma, J. Luo, Y. Zhang, J. Fu, C. Li and N. Yang, Hydrodeoxygenation of 2-methoxy phenol: Effects of catalysts and process parameters on conversion and products selectivity, *J. Energy Inst.*, 2020, **93**, 1527–1534, DOI: 10.1016/j.joei.2020.01.015.

98 Z. Luo, Z. Zheng, Y. Wang, G. Sun, H. Jiang and C. Zhao, Hydrothermally stable Ru/HZSM-5-catalyzed selective hydrogenolysis of lignin-derived substituted phenols to bio-arenes in water, *Green Chem.*, 2016, **18**, 5845–5858, DOI: 10.1039/C6GC01971D.

99 C. Zhang, C. Jia, Y. Cao, Y. Yao, S. Xie, S. Zhang and H. Lin, Water-assisted selective hydrodeoxygenation of phenol to benzene over the Ru composite catalyst in the biphasic process, *Green Chem.*, 2019, **21**, 1668–1679, DOI: 10.1039/C8GC04017F.

100 E. Aliu, A. Hart and J. Wood, Mild-Temperature hydrodeoxygenation of vanillin a typical bio-oil model compound to Creosol a potential future biofuel, *Catal. Today*, 2021, **379**, 70–79, DOI: 10.1016/j.cattod.2020.05.066.

101 J. Wang and W. Wan, The effect of substrate concentration on biohydrogen production by using kinetic models, *Sci. China, Ser. B: Chem.*, 2008, **51**, 1110–1117, DOI: 10.1007/s11426-008-0104-6.

102 M. Xiang and D. Wu, Highly selective catalytic conversion of lignin-derived phenolic compounds to cycloalkanes over a hierarchically structured zeolite catalyst, *J. Mater. Sci.*, 2019, **54**, 2940–2959, DOI: 10.1007/s10853-018-3057-y.

103 G. A. Somorjai, K. R. McCrea and J. Zhu, Active Sites in Heterogeneous Catalysis: Development of Molecular Concepts and Future Challenges, *Top. Catal.*, 2002, **18**, 157–166, DOI: 10.1023/A:1013874202404.

104 M. Žula, M. Grilc and B. Likozar, Hydrocracking, hydrogenation and hydro-deoxygenation of fatty acids, esters and glycerides: Mechanisms, kinetics and transport phenomena, *Chem. Eng. J.*, 2022, **444**, 136564, DOI: 10.1016/j.cej.2022.136564.

105 Y. Zhao, J. Zhan, R. Hu, G. Luo, J. Fan, J. H. Clark and S. Zhang, Water-assisted catalytic transfer hydrogenation of guaiacol to cyclohexanol over Ru/NiAl2O4, *Chem. Eng. J.*, 2024, **485**, 149934, DOI: 10.1016/j.cej.2024.149934.

106 M. Zhou, F. Ge, J. Li, H. Xia, J. Liu, J. Jiang, C. Chen, J. Zhao and X. Yang, Catalytic Hydrodeoxygenation of Guaiacol to Cyclohexanol over Bimetallic NiMo-MOF-Derived Catalysts, *Catalysts*, 2022, **12**, 371, DOI: 10.3390/catal12040371.

107 W. Song, Y. Liu, E. Baráth, C. Zhao and J. A. Lercher, Synergistic effects of Ni and acid sites for hydrogenation and C–O bond cleavage of substituted phenols, *Green Chem.*, 2015, **17**, 1204–1218, DOI: 10.1039/C4GC01798F.

108 F. Alshehri, C. Feral, K. Kirkwood and S. D. Jackson, Low temperature hydrogenation and hydrodeoxygenation of oxygen-substituted aromatics over Rh/silica: part 1: phenol, anisole and 4-methoxyphenol, *React. Kinet., Mech. Catal.*, 2019, **128**, 23–40, DOI: 10.1007/s11144-019-01630-9.

109 M. Zhou, J. Ye, P. Liu, J. Xu and J. Jiang, Water-Assisted Selective Hydrodeoxygenation of Guaiacol to Cyclohexanol over Supported Ni and Co Bimetallic Catalysts, *ACS Sustainable Chem. Eng.*, 2017, **5**, 8824–8835, DOI: 10.1021/acssuschemeng.7b01615.

110 D. E. Pérez-Estrada, M. A. Sernaqué-Villagómez, L. H. Molina-Conde, A. Suárez-Méndez, R. Mendoza-Cruz and T. E. Klimova, A comparison of Ni, Pt, and NiPt catalysts supported on SBA-15 in anisole hydrodeoxygenation: Exploring the effect of platinum addition to a nickel catalyst, *MRS Commun.*, 2024, **14**, 1191–1200, DOI: 10.1557/s43579-024-00581-0.

111 C. W. Park, J. W. Kim, H. U. Kim, Y.-K. Park, S. S. Lam, J.-M. Ha and J. Jae, Bimetallic Ni-Re catalysts for the efficient hydrodeoxygenation of biomass-derived phenols, *Int. J. Energy Res.*, 2021, **45**, 16349–16361, DOI: 10.1002/er.6882.

112 O. U. Valdés-Martínez, C. E. Santolalla-Vargas, V. Santes, J. A. de los Reyes, B. Pawelec and J. L. G. Fierro, Influence of calcination on metallic dispersion and support interactions for NiRu/TiO2 catalyst in the hydrodeoxygenation of phenol, *Catal. Today*, 2019, **329**, 149–155, DOI: 10.1016/j.cattod.2018.11.007.

113 R. Guo, Y. Zeng, L. Lin, D. Hu, C. Lu, S. Conroy, S. Zhang, C. Zeng, H. Luo, Z. Jiang, X. Zhang, X. Tu and K. Yan, CO2-Assisted Controllable Synthesis of PdNi Nanoalloys for Highly Selective Hydrogenation of Biomass-Derived 5-Hydroxymethylfurfural, *Angew. Chem., Int. Ed.*, 2025, **64**, e202418234, DOI: 10.1002/anie.202418234.

114 B. Chen, F. Li, Z. Huang and G. Yuan, Tuning catalytic selectivity of liquid-phase hydrogenation of furfural *via* synergistic effects of supported bimetallic catalysts, *Appl. Catal., A*, 2015, **500**, 23–29, DOI: 10.1016/j.apcata.2015.05.006.

115 D. E. Pérez-Estrada, H. Vargas-Villagrán, R. Mendoza-Cruz and T. E. Klimova, Hydrodeoxygenation of anisole over SBA-15-supported Ni, Pd, and Pt mono- and bimetallic catalysts: effect of the metal's nature on catalytic activity and selectivity, *Nanoscale*, 2024, **16**, 11575–11591, DOI: 10.1039/D4NR01222D.

116 K. W. Cheah, M. J. Taylor, A. Osatiashtiani, S. K. Beaumont, D. J. Nowakowski, S. Yusup, A. V. Bridgwater and G. Kyriakou, Monometallic and bimetallic catalysts based on Pd, Cu and Ni for hydrogen transfer deoxygenation of a prototypical fatty acid to diesel range hydrocarbons, *Catal. Today*, 2020, **355**, 882–892, DOI: 10.1016/j.cattod.2019.03.017.

117 D. E. Pérez-Estrada, A. Suárez-Méndez, M. Betancourt-Aldana, L. H. Molina-Conde, F. González-Zavala, L. Huerta, X. Bokhimi and T. E. Klimova, Searching for

the optimum Pt loading in bimetallic PtXNi/SBA-15 catalysts for hydrodeoxygenation, *MRS Commun.*, 2024, **14**, 1224–1234, DOI: 10.1557/s43579-024-00635-3.

118 Y. Tian, L. Guo, C. Qiao, Z. Sun, Y. Yamauchi and S. Liu, Dynamics-driven tailoring of sub-nanometric Pt-Ni bimetals confined in hierarchical zeolite for catalytic hydrodeoxygenation, *Appl. Catal., B*, 2023, **336**, 122945, DOI: 10.1016/j.apcatb.2023.122945.

119 R. Rios-Escobedo, E. Ortiz-Santos, J. A. Colín-Luna, J. N. Díaz de León, P. del Angel, J. Escobar and J. A. de los Reyes, Anisole Hydrodeoxygenation: A Comparative Study of Ni/TiO2-ZrO2 and Commercial TiO2 Supported Ni and NiRu Catalysts, *Top. Catal.*, 2022, **65**, 1448–1461, DOI: 10.1007/s11244-022-01662-x.

120 C. Zhao, J. He, A. A. Lemonidou, X. Li and J. A. Lercher, Aqueous-phase hydrodeoxygenation of bio-derived phenols to cycloalkanes, *J. Catal.*, 2011, **280**, 8–16, DOI: 10.1016/j.jcat.2011.02.001.

121 M. Lu, H. Du, B. Wei, J. Zhu, M. Li, Y. Shan, J. Shen and C. Song, Hydrodeoxygenation of Guaiacol on Ru Catalysts: Influence of TiO2–ZrO2 Composite Oxide Supports, *Ind. Eng. Chem. Res.*, 2017, **56**, 12070–12079, DOI: 10.1021/acs.iecr.7b02569.

122 Y. Shao, Q. Xia, L. Dong, X. Liu, X. Han, S. F. Parker, Y. Cheng, L. L. Daemen, A. J. Ramirez-Cuesta, S. Yang and Y. Wang, Selective production of arenes via direct lignin upgrading over a niobium-based catalyst, *Nat. Commun.*, 2017, **8**, 16104, DOI: 10.1038/ncomms16104.

123 J. A. Hunns, L. J. Durndell, X. Zhang, M. Konarova, A. F. Lee and K. Wilson, Tuning Acid-Metal Synergy in m-Cresol Hydrodeoxygenation over Bifunctional Pt/Aluminosilicate Catalysts, *ACS Catal.*, 2024, **14**, 7052–7061, DOI: 10.1021/acscatal.4c00402.